JPL Publication 92-14, Vol. 2

Summaries of the Third Annual JPL Airborne Geoscience Workshop June 1–5, 1992

Volume 2. TIMS Workshop

Vincent J. Realmuto
Editor

June 1, 1992

National Aeronautics and Space Administration

Jet Propulsion Laboratory
California Institute of Technology
Pasadena, California

[redacted]

JPL Publication 92-14, Vol. 2

Summaries of the Third Annual JPL Airborne Geoscience Workshop June 1–5, 1992

Volume 2. TIMS Workshop

Vincent J. Realmuto
Editor

June 1, 1992

National Aeronautics and
Space Administration

Jet Propulsion Laboratory
California Institute of Technology
Pasadena, California

This publication was prepared by the Jet Propulsion Laboratory, California Institute of Technology, under a contract with the National Aeronautics and Space Administration.

ABSTRACT

This publication contains the preliminary agenda and summaries for the Third Annual JPL Airborne Geoscience Workshop, held at the Jet Propulsion Laboratory, Pasadena, California, on June 1–5, 1992. This main workshop is divided into three smaller workshops as follows:

- The Airborne Visible/Infrared Imaging Spectrometer (AVIRIS) workshop, on June 1 and 2. The summaries for this workshop appear in Volume 1.
- The Thermal Infrared Multispectral Scanner (TIMS) workshop, on June 3. The summaries for this workshop appear in Volume 2.
- The Airborne Synthetic Aperture Radar (AIRSAR) workshop, on June 4 and 5. The summaries for this workshop appear in Volume 3.

CONTENTS

Volume 1: AVIRIS Workshop

omit TO P.1

AGENDA

THIRD ANNUAL JPL AIRBORNE GEOSCIENCE WORKSHOP: AIRBORNE VISIBLE/INFRARED IMAGING SPECTROMETER (AVIRIS)

June 1 and 2, 1992
Von Karman Auditorium
Jet Propulsion Laboratory
Pasadena, California 91109

MONDAY, JUNE 1, 1992

7:15 a.m.	Shuttle bus departs Pasadena Ritz-Carlton Hotel for JPL.
7:30 a.m.	Registration and continental breakfast at JPL.
8:00 a.m.	Welcome
8:30 a.m.	In-Flight Calibration of the Spectral and Radiometric Characteristics of AVIRIS in 1991 *Robert O. Green, James E. Conel, Carol J. Bruegge, Jack S. Margolis, Veronique Carrere, Gregg Vane, and Gordon Hoover*
9:00 a.m.	Using AVIRIS Images To Measure Temporal Trends in Abundance of Photosynthetic and Nonphotosynthetic Canopy Components *Susan L. Ustin, Milton O. Smith, Dar Roberts, John A. Gamon, and Christopher B. Field*
9:30 a.m.	Unmixing AVIRIS Data To Provide a Method for Vegetation Fraction Subtraction *J.A. Zamudio*
10:00 a.m.	Break
10:30 a.m.	Mapping the Mineralogy and Lithology of Canyonlands, Utah With Imaging Spectrometer Data and the Multiple Spectral Feature Mapping Algorithm *Roger N. Clark, Gregg A. Swayze, and Andrea Gallagher*
11:00 a.m.	Spatial Resolution and Cloud Optical Thickness Retrievals *Rand E. Feind, Sundar A. Christopher, and Ronald M. Welch*
11:30 a.m.	Evaluation of Spatial Productivity Patterns in an Annual Grassland During an AVIRIS Overflight *John A. Gamon, Christopher B. Field, and Susan L. Ustin*
12:00 noon	Lunch
1:00 p.m.	Hyperspectral Modeling for Extracting Aerosols From Aircraft/Satellite Data *G. Daniel Hickman and Michael J. Duggin*
1:30 p.m.	The Spectral Image Processing System (SIPS)—Software for Integrated Analysis of AVIRIS Data *F.A. Kruse, A.B. Lefkoff, J.W. Boardman, K.B. Heidebrecht, A.T. Shapiro, P.J. Barloon, and A.F.H. Goetz*

THIRD ANNUAL JPL AIRBORNE GEOSCIENCE WORKSHOP: AIRBORNE VISIBLE/INFRARED IMAGING SPECTROMETER (AVIRIS)

2:00 p.m. First Results From Analysis of Coordinated AVIRIS, TIMS, and ISM (French) Data for the Ronda (Spain) and Beni Bousera (Morocco) Peridotites
J.F. Mustard, S. Hurtrez, P. Pinet, and C. Sotin

2:30 p.m. AVIRIS Study of Death Valley Evaporite Deposits Using Least-Squares Band-Fitting Methods
J.K. Crowley and R.N. Clark

3:00 p.m. Break

3:30 p.m. A Field Measure of the "Shade" Fraction
Alan R. Gillespie, Milton O. Smith, and Donald E. Sabol

4:00 p.m. A Linear Spectral Matching Technique for Retrieving Equivalent Water Thickness and Biochemical Constituents of Green Vegetation
Bo-Cai Gao and Alexander F.H. Goetz

4:30 p.m. Poster Previews

5:00 p.m. Poster Previews

5:30 p.m. End of session.

5:45 p.m. Shuttle bus departs JPL for the Pasadena Ritz-Carlton Hotel.

6:30 p.m. Reception and poster sessions at the Pasadena Ritz-Carlton Hotel.

9:00 p.m. Close of reception and poster sessions.

AGENDA

THIRD ANNUAL JPL AIRBORNE GEOSCIENCE WORKSHOP:
POSTER SESSION

Monday, June 1, 1992
6:30 to 9:00 p.m.
Pasadena Ritz-Carlton Hotel

1. Use of AVIRIS Data to the Definition of Optimised Specifications for Land Applications With Future Spaceborne Imaging Spectrometers
J. Bodechtel

2. Primary Studies of Trace Quantities of Green Vegetation in Mono Lake Area Using 1990 AVIRIS Data
Zhikang Chen, Chris D. Elvidge, and David P. Groeneveld

3. JPL Activities on Development of Acousto-Optic Tunable Filter Imaging Spectrometer
Li-Jen Cheng, Tien-Hsin Chao, and George Reyes

4. Measuring Dry Plant Residues in Grasslands: A Case Study Using AVIRIS
Michael Fitzgerald and Susan L. Ustin

5. Analysis of AVIRIS San Pedro Channel Data: Methods and Applications
Richard B. Frost

6. Tracking Photosynthetic Efficiency With Narrow-Band Spectroradiometry
John A. Gamon and Christopher B. Field

7. Separation of Cirrus Cloud From Clear Surface From AVIRIS Data Using the 1.38-μm Water Vapor Band
Bo-Cai Gao and Alexander F.H. Goetz

8. Software for the Derivation of Scaled Surface Reflectances From AVIRIS Data
Bo-Cai Gao, Kathleen Heidebrecht, and Alexander F.H. Goetz

9. Integrating Remote Sensing Techniques at Cuprite, Nevada: AVIRIS, Thematic Mapper, and Field Spectroscopy
Bradley Hill, Greg Nash, Merrill Ridd, Phoebe Hauff, and Phil Ebel

10. Evaluation of AVIRISwiss-91 Campaign Data
K.I. Itten, P. Meyer, K. Staenz, T. Kellenberger, and M. Schaepman

11. AVIRIS Investigator's Guide
Howell Johnson

12. Oregon Transect: Comparison of Leaf-Level Reflectance With Canopy-Level and Modelled Reflectance
Lee F. Johnson, Frederic Baret, and David L. Peterson

13. AVIRIS as a Tool for Carbonatite Exploration: Comparison of SPAM and Mbandmap Data Analysis Methods
Marguerite J. Kingston and James K. Crowley

14. Expert System-Based Mineral Mapping Using AVIRIS
F.A. Kruse, A.B. Lefkoff, and J.B. Dietz

THIRD ANNUAL JPL AIRBORNE GEOSCIENCE WORKSHOP:
MONDAY POSTER SESSION (CONTINUED)

15. The EARSEC Programme in Relation to the 1991 MAC-Europe Campaign
Wim J. Looyen, Jean Verdebout, Benny M. Sorensen, Giancarlo Maracci, Guido Schmuck, and Alois J. Sieber

16. Preliminary Statistical Analysis of AVIRIS/TMS Data Acquired Over the Matera Test Site
Stefania Mattei and Sergio Vetrella

17. AVIRIS Data and Neural Networks Applied to an Urban Ecosystem
Merrill K. Ridd, Niles D. Ritter, Nevin A. Bryant, and Robert O. Green

18. Temporal Variation in Spectral Detection Thresholds of Substrate and Vegetation in AVIRIS Images
Donald E. Sabol, Jr., Dar Roberts, Milton Smith, and John Adams

19. Discussion of Band Selection and Methodologies for the Estimation of Precipitable Water Vapour From AVIRIS Data
Dena Schanzer and Karl Staenz

20. Abundance Recovery Error Analysis Using Simulated AVIRIS Data
William W. Stoner, Joseph C. Harsanyi, William H. Farrand, and Jennifer A. Wong

21. Multitemporal Diurnal AVIRIS Images of a Forested Ecosystem
Susan L. Ustin, Milton O. Smith, and John B. Adams

22. A Comparison of LOWTRAN-7 Corrected Airborne Visible/Infrared Imaging Spectrometer (AVIRIS) Data With Ground Spectral Measurements
Pengyang Xu and Ronald Greeley

23. Discrimination Among Semi-Arid Landscape Endmembers Using the Spectral Angle Mapper (SAM) Algorithm
Roberta H. Yuhas, Alexander F.H. Goetz, and Joe W. Boardman

24. Empirical Relationships Among Atmospheric Variables From Rawinsonde and Field Data as Surrogates for AVIRIS Measurements: Estimation of Regional Land Surface Evapotranspiration
James E. Conel, Gordon Hoover, Anne Nolin, Ron Alley, and Jack Margolis

AGENDA

THIRD ANNUAL JPL AIRBORNE GEOSCIENCE WORKSHOP: AIRBORNE VISIBLE/INFRARED IMAGING SPECTROMETER (AVIRIS)

June 1 and 2, 1992
Von Karman Auditorium
Jet Propulsion Laboratory
Pasadena, California 91109

TUESDAY, JUNE 2, 1992

7:15 a.m. Shuttle bus departs Pasadena Ritz-Carlton Hotel for JPL.

7:30 a.m. Registration and continental breakfast at JPL.

8:00 a.m. Mapping the Spectral Variability in Photosynthetic and Non-Photosynthetic Vegetation, Soils and Shade Using AVIRIS
Dar A. Roberts, Milton O. Smith, Donald E. Sabol, John B. Adams, and Susan Ustin

8:30 a.m. Volcanic Thermal Features Observed by AVIRIS
Clive Oppenheimer, David Pieri, Veronique Carrere, Michael Abrams, David Rothery, and Peter Francis

9:00 a.m. Retrieval of Biophysical Parameters With AVIRIS and ISM—The Landes Forest, South West France
F. Zagolski, J.P. Gastellu-Etchegorry, E. Mougin, G. Giordano, G. Marty, T. Le Toan, and A. Beaudoin

9:30 a.m. Ground-Truthing AVIRIS Mineral Mapping at Cuprite, Nevada
Gregg Swayze, Roger N. Clark, Fred Kruse, Steve Sutley, and Andrea Gallagher

10:00 a.m. Break

10:30 a.m. Exploring the Remote Sensing of Foliar Biochemical Concentrations With AVIRIS Data
Geoffrey M. Smith and Paul J. Curran

11:00 a.m. Seasonal and Spatial Variations in Phytoplanktonic Chlorophyll in Eutrophic Mono Lake, California, Measured With the Airborne Visible and Infrared Imaging Spectrometer (AVIRIS)
John M. Melack and Mary Gastil

11:30 a.m. AVIRIS Calibration and Application in Coastal Oceanic Environments
Kendall L. Carder

12:00 noon Lunch

1:00 p.m. Mapping Vegetation Types With the Multiple Spectral Feature Mapping Algorithm in Both Emission and Absorption
Roger N. Clark, Gregg A. Swayze, Christopher Koch, and Cathy Ager

THIRD ANNUAL JPL AIRBORNE GEOSCIENCE WORKSHOP: AIRBORNE VISIBLE/INFRARED IMAGING SPECTROMETER (AVIRIS)

1:30 p.m. Multiple Dataset Water-Quality Analyses in the Vicinity of an Ocean Wastewater Plume
Michael Hamilton, Curtiss O. Davis, W. Joseph Rhea, and Jeannette van den Bosch

2:00 p.m. MAC Europe 91: Evaluation of AVIRIS, GER Imaging Spectrometry Data for the Land Application Testsite Oberpfaffenhofen
F. Lehmann, R. Richter, H. Rothfuss, K. Werner, P. Hausknecht, A. Müller, and P. Strobl

2:30 p.m. Using Endmembers in AVIRIS Images To Estimate Changes in Vegetative Biomass
Milton O. Smith, John B. Adams, Susan L. Ustin, and Dar A. Roberts

3:00 p.m. Break

3:30 p.m. Atmospheric Correction of AVIRIS Data in Ocean Waters
Gregory Terrie and Robert Arnone

4:00 p.m. The 1991 AVIRIS/POLDER Experiment in Camargue, France
F. Baret, C. Leprieur, S. Jacquemoud, V. Carrère, X.F. Gu, M. Steven, V. Vanderbilt, J.F. Hanocq, S. Ustin, G. Rondeaux, C. Daughtry, L. Biehl, R. Pettigrew, D. Modro, H. Horoyan, T. Sarto, C. Despontin, and H. Razafindraibe

4:30 p.m. AVIRIS Sensor and Ground Data System: Status and Plans
Thomas Chrien and Earl Hansen

5:00 p.m. Wrap up.

5:30 p.m. End of AVIRIS Workshop.

5:45 p.m. Shuttle bus departs JPL for the Pasadena Ritz-Carlton Hotel.

AGENDA

THIRD ANNUAL JPL AIRBORNE GEOSCIENCE WORKSHOP: THERMAL INFRARED MULTISPECTRAL SCANNER (TIMS)

June 3, 1992
Von Karman Auditorium
Jet Propulsion Laboratory
Pasadena, California 91109

WEDNESDAY, JUNE 3, 1992

7:15 a.m.	Shuttle bus departs Pasadena Ritz-Carlton Hotel for JPL.
7:30 a.m.	Registration and continental breakfast at JPL.
8:00 a.m.	Welcome
8:30 a.m.	TIMS Performance Evaluation Summary *Bruce Spiering, G. Meeks, J. Anderson, S. Jaggi, and S. Kuo*
	A Quantitative Analysis of TIMS Data Obtained on the Learjet 23 at Various Altitudes *S. Jaggi*
	Analysis of TIMS Performance Subjected to Simulated Wind Blast *S. Jaggi and S. Kuo*
9:30 a.m.	Sensitivity of Blackbody Reference Panels to Wind Blast *Gordon Hoover*
10:00 a.m.	Break
10:30 a.m.	Preliminary Analysis of TIMS Performance on the ER-2 *S.J. Hook, V.J. Realmuto, and R.E. Alley*
11:00 a.m.	Comparison of Preliminary Results From Airborne ASTER Simulator (AAS) With TIMS Data *Yoshiaki Kannari, Franklin Mills, Hiroshi Watanabe, Teruya Ezaka, Tatsuhiko Narita, and Sheng-Huei Chang*
11:30 a.m.	Simulation of ASTER Data Using AVIRIS Images *Michael Abrams*
12:00 noon	Lunch
1:00 p.m.	Application of Split Window Technique to TIMS Data *Tsuneo Matsunaga, Shuichi Rokugawa, and Yoshinori Ishii*
1:30 p.m.	Atmospheric Corrections for TIMS Estimated Emittance *T.A. Warner and D.W. Levandowski*
2:00 p.m.	An Algorithm for the Estimation of Bounds on the Emissivity and Temperatures From Thermal Multispectral Airborne Remotely Sensed Data *S. Jaggi, D. Quattrochi, and R. Baskin*

THIRD ANNUAL JPL AIRBORNE GEOSCIENCE WORKSHOP: THERMAL INFRARED MULTISPECTRAL SCANNER (TIMS)

2:30 p.m. Multi-Resolution Processing for Fractal Analysis of Airborne Remotely Sensed Data
S. Jaggi, D. Quattrochi, and N. Lam

3:00 p.m. Break

3:30 p.m. Preliminary Analysis of Thermal-Infrared Multispectral Scanner Data of the Iron Hill, Colorado Carbonatite-Alkalic Rock Complex
Lawrence C. Rowan, Kenneth Watson, and Susanne H. Miller

4:00 p.m. The Use of TIMS for Mapping Different Pahoehoe Surfaces: Mauna Iki, Kilauea
Scott K. Rowland

4:30 p.m. Ejecta Patterns of Meteor Crater, Arizona Derived From the Linear Un-Mixing of TIMS Data and Laboratory Thermal Emission Spectra
Michael S. Ramsey and Philip R. Christensen

5:00 p.m. The Use of TIMS Data To Estimate the SO_2 Concentrations of Volcanic Plumes: A Case Study at Mount Etna, Sicily
Vincent J. Realmuto

5:30 p.m. End of TIMS Workshop.

5:45 p.m. Shuttle bus departs JPL for the Pasadena Ritz-Carlton Hotel.

AGENDA

THIRD ANNUAL JPL AIRBORNE GEOSCIENCE WORKSHOP:
AIRBORNE SYNTHETIC APERTURE RADAR
(AIRSAR)

June 4 and 5, 1992
Von Karman Auditorium
Jet Propulsion Laboratory
Pasadena, California 91109

THURSDAY, JUNE 4, 1992

7:15 a.m. Shuttle bus departs Pasadena Ritz-Carlton Hotel for JPL.

7:30 a.m. Registration and continental breakfast at JPL.

8:00 a.m. Welcome

8:30 a.m. The NASA/JPL Three-Frequency AIRSAR System
J. van Zyl, R. Carande, Y. Low, T. Miller, and K. Wheeler

9:00 a.m. A Snow Wetness Retrieval Algorithm for SAR
Jiancheng Shi and Jeff Dozier

9:30 a.m. Comparison of JPL-AIRSAR and DLR E-SAR Images from the MAC Europe '91 Campaign Over Testsite Oberpfaffenhofen: Frequency and Polarization Dependent Backscatter Variations From Agricultural Fields
C. Schmullius and J. Nithack

10:00 a.m. Break

10:30 a.m. Monitoring Environmental State of Alaskan Forests With AIRSAR
Kyle C. McDonald, JoBea Way, Eric Rignot, Cindy Williams, Les Viereck, and Phylis Adams

11:00 a.m. Comparison of Modeled Backscatter With SAR Data at P-Band
Yong Wang, Frank W. Davis, and John M. Melack

11:30 a.m. SAR Backscatter From Coniferous Forest Gaps
John L. Day and Frank W. Davis

12:00 noon Lunch

1:00 p.m. Panel Discussion on Future Emphasis of the AIRSAR System
J. van Zyl, Moderator

1:30 p.m. Retrieval of Pine Forest Biomass Using JPL AIRSAR Data
A. Beaudoin, T. Le Toan, F. Zagolski, C.C. Hsu, H.C. Han, and J.A. Kong

2:00 p.m. Characterization of Wetland, Forest, and Agricultural Ecosystems in Belize With Airborne Radar (AIRSAR)
Kevin O. Pope, Jose Maria Rey-Benayas, and Jack F. Paris

2:30 p.m. Strategies for Detection of Floodplain Inundation With Multi-Frequency Polarimetric SAR
Laura L. Hess and John M. Melack

THIRD ANNUAL JPL AIRBORNE GEOSCIENCE WORKSHOP: AIRBORNE SYNTHETIC APERTURE RADAR (AIRSAR)

3:00 p.m.	Break
3:30 p.m.	Supervised Fully Polarimetric Classification of the Black Forest Test Site: From MAESTRO1 to MAC Europe *G. De Grandi, C. Lavalle, H. De Groof, and A. Sieber*
4:00 p.m.	Relating Multifrequency Radar Backscattering to Forest Biomass: Modeling and AIRSAR Measurement *Guoqing Sun and K. Jon Ranson*
4:30 p.m.	Poster Previews
5:00 p.m.	Poster Previews
5:30 p.m.	End of session.
5:45 p.m.	Shuttle bus departs JPL for the Pasadena Ritz-Carlton Hotel.
6:30 p.m.	Reception and poster sessions at the Pasadena Ritz-Carlton Hotel.
9:00 p.m.	Close of reception and poster sessions.

AGENDA

THIRD ANNUAL JPL AIRBORNE GEOSCIENCE WORKSHOP:
POSTER SESSION

Thursday, June 4, 1992
6:30 to 9:00 p.m.
Pasadena Ritz-Carlton Hotel

1. Processing of AIRSAR Polarimetric Data for Soil Moisture Estimation Over Mahantango Watershed Area
K.S. Rao

2. Evaluation of Polarimetric SAR Parameters for Soil Moisture Retrieval
Jiancheng Shi, Jakob J. van Zyl, and Edwin T. Engman

3. Interaction Types and Their Like-Polarization Phase-Angle Difference Signatures
Jack F. Paris

4. Application of Modified VICAR/IBIS GIS to Analysis of July 1991 Flevoland AIRSAR Data
L. Norikane, B. Broek, and A. Freeman

5. Radar Analysis and Visualization Environment (RAVEN): Software for Polarimetric Radar Analysis
K.S. Kierein-Young, A.B. Lefkoff, and F.A. Kruse

6. Measuring Ocean Coherence Time With Dual-Baseline Interferometry
Richard E. Carande

7. A Bibliography of Global Change, Airborne Science, 1985-1991
Edwin J. Sheffner and James G. Lawless

8. ATTIRE (Analytical Tools for Thermal Infrared Engineering)—A Thermal Sensor Simulation Package
S. Jaggi

9. Kilauea Data Set Complied for Distribution on Compact Disc
Lori Glaze, George Karas, Sonia Chernobieff, Elsa Abbott, and Earnie Paylor

10. The JPL Spectral Library 0.4 to 2.5 Micrometers
Simon J. Hook, Cindy I. Grove, and Earnest D. Paylor II

11. Lossless Compression of AVIRIS Data: Comparison of Methods and Instrument Constraints
R.E. Roger, J.F. Arnold, M.C. Cavenor, and J.A. Richards

12. Simulation of AVHRR-K Band Ratios With AVIRIS
Melanie A. Wetzel and Ronald M. Welch

13. Soil Conservation Applications With C-Band SAR
B. Brisco, R.J. Brown, J. Naunheimer, and D. Bedard

14. Comparison of Edges Detected at Different Polarisations in MAESTRO Data
Ronald G. Caves, Peter J. Harley, and Shaun Quegan

15. Identification of Erosion Hazards in a Mediterranean Environment
M. Altherr, J. Hill, and W. Mehl

AGENDA

THIRD ANNUAL JPL AIRBORNE GEOSCIENCE WORKSHOP:
AIRBORNE SYNTHETIC APERTURE RADAR
(AIRSAR)

June 4 and 5, 1992
Von Karman Auditorium
Jet Propulsion Laboratory
Pasadena, California 91109

FRIDAY, JUNE 5, 1992

7:15 a.m. Shuttle bus departs Pasadena Ritz-Carlton Hotel for JPL.

7:30 a.m. Registration and continental breakfast at JPL.

8:00 a.m. Oceanic Features Detected by SAR in the Mediterranean Sea During the MAC Europe '91 Campaign
Werner Alpers

8:30 a.m. SAR Observations in the Gulf of Mexico
David Sheres

9:00 a.m. Investigation of AIRSAR Signatures of the Gulf Stream
G.R. Valenzuela, J.S. Lee, D.L. Schuler, G.O. Marmorino, F. Askari, K. Hoppel, J.A.C. Kaiser, and W.C. Keller

9:30 a.m. Mapping of Sea Bottom Topography
C.J. Calkoen, G.J. Wensink, and G.H.F.M. Hesselmans

10:00 a.m. Break

10:30 a.m. Sea Bottom Topography Imaging With SAR
M.W.A. van der Kooij, G.J. Wensink, and J. Vogelzang

11:00 a.m. AIRSAR Surveys of Upper-Ocean Fronts Off California and Hawaii
P. Flament

11:30 a.m. Preliminary Results of Polarization Signatures for Glacial Moraines in the Mono Basin, Eastern Sierra Nevada
Richard R. Forster, Andrew N. Fox, and Bryan Isacks

12:00 noon Lunch

1:00 p.m. Detecting Surface Roughness Effects on the Atmospheric Boundary Layer Via AIRSAR Data: A Field Experiment in Death Valley, California
Dan G. Blumberg and Ronald Greeley

1:30 p.m. Extraction of Quantitative Surface Characteristics From AIRSAR Data for Death Valley, California
K.S. Kierein-Young and F.A. Kruse

2:00 p.m. The TOPSAR Interferometric Radar Topographic Mapping Instrument
Howard A. Zebker, Søren N. Madsen, Jan Martin, Giovanni Alberti, Sergio Vetrella, and Alessandro Cucci

THIRD ANNUAL JPL AIRBORNE GEOSCIENCE WORKSHOP:
AIRBORNE SYNTHETIC APERTURE RADAR
(AIRSAR)

2:30 p.m. Evaluation of the TOPSAR Performance by Using Passive and Active Calibrators
G. Alberti, A. Moccia, S. Ponte, and S. Vetrella

3:00 p.m. Break

3:30 p.m. Fitting a Three-Component Scattering Model to Polarimetric SAR Data
A. Freeman and S. Durden

4:00 p.m. Application of Symmetry Properties to Polarimetric Remote Sensing With JPL AIRSAR Data
S.V. Nghiem, S.H. Yueh, R. Kwok, and F.K. Li

4:30 p.m. External Calibration of Polarimetric Radar Images Using Distributed Targets
Simon H. Yueh, S.V. Nghiem, and R. Kwok

5:00 p.m. Wrap up.

5:30 p.m. End of AIRSAR Workshop.

5:45 p.m. Shuttle bus departs JPL for the Pasadena Ritz-Carlton Hotel.

TIMS PERFORMANCE EVALUATION SUMMARY

BRUCE SPIERING, G. MEEKS, J. ANDERSON, S. JAGGI, S. KUO
NASA/STENNIS SPACE CENTER
STENNIS SPACE CENTER, MS 39529

1. PURPOSE

The purpose of this effort was to investigate the TIMS operation under various conditions to determine what effect, if any, there is on the TIMS performance. This effort was undertaken because of reports from investigators that the TIMS is not performing as expected when flown on the ARC C-130. This effort was initiated with a meeting at SSC with representatives from SSC, JPL and ARC.

2. PROBLEM DEFINITION

The problem with the TIMS performance on the C-130 has been characterized in different ways. The primary problem seems to be as follows: Given a blackbody temperature reading from the blackbody controller, different digital count values can be obtained from the blackbody surface as measured by the TIMS, under different conditions encountered on the C-130. These differences result in incorrect surface temperatures computed from the data. Surface temperatures computed from TIMS data collected on the C-130 can be as much as 5C different than the ground truth data.

3. EXPERIMENTAL PLAN

A series of experiments were planned which would systematically illuminate possible conditions which have a measurable effect on the TIMS performance. The hypothesis was that ambient temperature and wind blast on the surface of the TIMS blackbodies was affecting the TIMS performance on the C-130.

The first experiment was a flight test with the TIMS installed on the SSC Learjet. The hypothesis was that ambient temperature and wind blast would affect the TIMS performance. Five flights at different altitudes were made over a large body of water. The data was distributed to three different investigators for analysis. A detailed analysis of the data is found in "A Quantitative Analysis of TIMS Data Obtained on the SSC/Learjet 23 at Various Altitudes.",S. Jaggi, and "TIMS Performance Evaluation Flight Over Ross P. Barnett Reservoir in the Pre-Dawn Hours of 1

February 1992",Palluconi,et.al.

The second experiment involved simulating wind blast on the surface of the TIMS blackbodies while the TIMS was operated in the lab. The hypothesis was that wind blast on the surface of the blackbodies, at various speeds and orientations would affect the TIMS performance. A detailed analysis of the data is found in "Analysis of TIMS Performance Subjected to Simulated Wind Blast",Jaggi,Kuo.

A third experiment is planned if necessary. This experiment will be to define a flight experiment on the C-130. This experiment will include measurement of environmental conditions at the TIMS entrance aperture.

4. FLIGHT TEST RESULTS SUMMARY

Beginning at 3AM CST, five flights were flown in sequence at altitudes of 2Km, 6Km, 12Km, 6Km, and 2Km over the Ross Barnett Reservoir near Jackson, MS. Radio-sonde data and water surface temperatures were acquired. Surface temperatures were acquired with both mercury thermometers and with a hand held radiometer. These measurements differed by approximately 2C over all the sample points.

The TIMS data used in the initial analysis were the high and low temperature outputs from the blackbody controller, the high and low digital counts from the surface of the blackbodies, and the temperature outputs from the two ambient temperature monitors on the TIMS. One of the ambient temperature monitors was located in the TIMS entrance aperture near the high blackbody and the other was attached to the outside of the spectrometer housing.

The four parameters obtained from the blackbodies were used to compute the slope and offset of the System Transfer Equation(STE). The ambient temperature measurements were compared to the data from each altitude. Surface temperatures were computed from the video data independently by each investigator. Each investigator chose to use different techniques to compute surface temperature.

The blackbody parameters and the ambient temperatures have been compared for the different altitudes. The computed temperatures have been

S2-43

189097

P-3

A QUANTITATIVE ANALYSIS OF TIMS DATA OBTAINED ON THE LEARJET 23 AT VARIOUS ALTITUDES

N94-16597

S. Jaggi

Lockheed Engineering & Sciences Company
Stennis Space Center, Mississippi 39529

Summary

A series of TIMS data acquisition flights were conducted on the NASA Learjet 23 at different altitudes over a test site. The objective was to monitor the performance of the TIMS (its estimation of the brightness temperatures of the ground scene) with increasing altitude. The results do not show any significant correlation between the brightness temperatures and the altitude. The analysis indicates that the estimation of the temperatures is a function of the accuracy of the atmospheric correction used for each altitude.

Five flights were flown in succession at altitudes of 2 km (low), 6 km (mid), 12 km (high), and then back again at 6 km and 2 km. The area selected was the Ross Barnett reservoir near Jackson, Mississippi. The mission was flown during the predawn hours of Feb. 1, 1992. Radiosonde data was collected for that duration to profile the characteristics of the atmosphere. Ground truth temperatures using thermometers and radiometers were also obtained over an area of the reservoir. The results of two independent runs of the radiometer data averaged 7.03 ± .70°C for the first run and 7.31 ± .88°C for the second run. Brightness temperatures were obtained for each channel for all flights. These were calculated by assuming the emissivity of the target to be 1.0 and computing the corresponding blackbody temperature given the upwelling ground radiance for each channel. Of particular interest were the temperatures corresponding to the region for which the ground truth data was available. Those regions were identified in each of the flights. The statistics of the raw video data, the corresponding radiance incident at the sensor, the upwelling ground radiance after it has been corrected for the atmosphere and finally the brightness temperatures were computed for those regions of each flight.

The results of the brightness temperature of the region from channel 5 of the TIMS - the band least affected by the column of water and ozone - do not reveal a significant variation with altitude. The temperature varied from a mean value of 7.26 ± .42 °C at 2 km, to 8.22 ± .45 °C at 6 km and to 8.35 ± .38 °C at 12 km. Considering the system accuracy of the TIMS sensor and the cumulative effect of the errors that can be introduced at various stages of the process of converting the raw data to brightness temperature, a variation of less than a degree between the temperatures obtained is not considered significant. The variation does not seem to be a function of the altitude as there is no continuous trend of change in temperature values from the low to the high altitudes. Rather, there seems to be a jump from the low altitude temperature to the mid and high altitude values, which are relatively close to each other,in spite of the high altitude being twice as high as the mid altitude.

In this paper, the methodology used to obtain the brightness temperatures is described. The results of each stage of data conversion are illustrated. Also included are statistics for all the channels at each altitude and graphs for results of analysis on channel 5.

compared to the ground truth data for the different altitudes. The temperature differential between the TIMS data and the ground truth data does not exceed 2C. The blackbody parameters, ambient temperature measurements and different altitudes show no significant correlation. Therefore the original hypothesis has been found to be false, i.e., when the TIMS is operated on the SSC Learjet, there are no measurable effects on TIMS performance due to ambient temperature or wind blast on the surface of the blackbodies.

5. TIMS LABORATORY WIND ANALYSIS RESULTS SUMMARY

The TIMS was operated in the lab with various configurations of wind directed at the surface of the blackbodies. At the time of this writing a maximum wind velocity of 40mph was achieved. Below approximately 30mph, very little effect was observed in TIMS performance. However, with wind speeds of 40mph, the TIMS continued to perform as designed. The data collected did not support the hypothesis that wind blast on the surface of the blackbodies under lab conditions adversely affected the TIMS performance.

6. TIMS PERFORMANCE ANALYSIS RESULTS SUMMARY

The data collected during these experiments indicates that the TIMS is a robust instrument. It can be operated under a wide range of conditions and still perform within its design goals.

At this time, it has not yet been determined if the experiments described above are sufficient to predict the performance of the TIMS on the ARC C-130. The third experiment has not yet been performed. It is believed that given a carefully defined and executed data acquisition mission, the TIMS can and will produce useful data when flown on the C-130.

Table 1 Digitized Raw Video

Ch#	Mean-sigma	Mean	Mean+sigma	sigma
1	53.57	54.45	55.33	0.88
2	53.00	53.77	54.54	0.77
3	54.34	55.06	55.78	0.72
4	54.89	55.48	56.07	0.59
5	55.25	55.91	56.57	0.66
6	54.81	56.09	57.37	1.28

Ch#	Mean-sigma	Mean	Mean+sigma	sigma
1	53.92	54.66	55.4	0.74
2	55.52	56.27	57.02	0.75
3	56.87	57.56	58.25	0.69
4	57.71	58.36	59.01	0.65
5	58.32	59.12	59.92	0.80
6	58.11	59.61	61.11	1.50

Ch#	Mean-sigma	Mean	Mean+sigma	sigma
1	55.79	56.50	57.21	0.71
2	57.54	58.20	58.86	0.66
3	57.44	58.09	58.74	0.65
4	57.15	57.74	58.33	0.59
5	59.56	60.20	60.84	0.64
6	59.60	60.84	62.08	1.24

Table 2 Radiance at Sensor

Ch#	Mean-sigma	Mean flux1	Mean+sigma	sigma
1	6107.271	6156.892	6206.513	49.62061
2	6476.706	6515.484	6554.263	38.77849
3	6704.340	6741.429	6778.518	37.08908
4	6968.603	6997.923	7027.243	29.31978
5	7002.743	7033.566	7064.390	30.82368
6	6777.586	6827.190	6876.794	49.60391

Ch#	Mean-sigma	Mean flux2	Mean+sigma	sigma
1	6013.600	6056.766	6099.933	43.16620
2	6499.201	6538.567	6577.933	39.36593
3	6741.725	6778.419	6815.114	36.69470
4	6986.802	7020.963	7055.125	34.16165
5	7060.608	7099.624	7138.639	39.01520
6	6819.643	6880.537	6941.430	60.89335

Ch#	Mean-sigma	Mean flux3	Mean+sigma	sigma
1	6059.631	6101.236	6142.842	41.60599
2	6510.972	6546.439	6581.909	35.46958
3	6706.780	6741.702	6776.624	34.92172
4	6813.435	6846.065	6878.696	32.63078
5	7044.588	7076.431	7108.273	31.84239
6	6810.463	6861.764	6913.068	51.30400

Table 3 Radiance from Ground

Ch#	Mean-sigma	Mean grd1	Mean+sigma	sigma
1	5926.766	6020.224	6113.682	93.458
2	6415.357	6492.179	6569.001	76.822
3	6656.563	6716.856	6777.148	60.292
4	6953.435	6998.664	7043.893	45.229
5	6998.044	7048.213	7098.381	50.168
6	6740.201	6817.743	6895.285	77.542

Ch#	Mean-sigma	Mean grd2	Mean+sigma	sigma
1	6016.547	6108.779	6201.011	92.232
2	6558.239	6618.023	6677.806	59.783
3	6787.691	6852.267	6916.842	64.575
4	7082.597	7150.960	7219.323	68.363
5	7109.192	7164.826	7220.461	55.635
6	6830.949	6922.543	7014.137	91.594

Ch#	Mean-sigma	Mean grd3	Mean+sigma	sigma
1	6250.651	6311.322	6371.993	60.671
2	6661.366	6704.410	6747.454	43.044
3	6896.086	6951.107	7006.128	55.021
4	7558.171	7604.735	7651.299	46.464
5	7134.094	7181.590	7229.085	47.495
6	6831.457	6902.734	6974.012	71.278

Table 4 Brightness Temperature

Ch#	Mean-sigma	Mean temp1	Mean+sigma	sigma
1	4.372	5.07	5.768	0.698
2	5.788	6.35	6.912	0.562
3	5.910	6.36	6.810	0.450
4	6.675	7.02	7.365	0.345
5	6.838	7.26	7.682	0.422
6	6.282	7.00	7.718	0.718

Ch#	Mean-sigma	Mean temp2	Mean+sigma	sigma
1	5.044	5.72	6.396	0.676
2	6.832	7.26	7.688	0.428
3	6.886	7.36	7.834	0.474
4	7.647	8.17	8.693	0.523
5	7.772	8.22	8.668	0.448
6	7.122	7.96	8.798	0.838

Ch#	Mean-sigma	Mean temp3	Mean+sigma	sigma
1	6.765	7.21	7.655	0.445
2	7.572	7.89	8.208	0.318
3	7.681	8.08	8.479	0.399
4	11.010	11.62	12.230	0.610
5	7.973	8.35	8.727	0.377
6	7.134	7.78	8.426	0.646

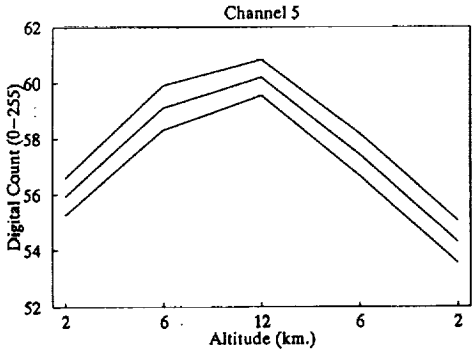

Variation of Ch#5 average video count with altitude.

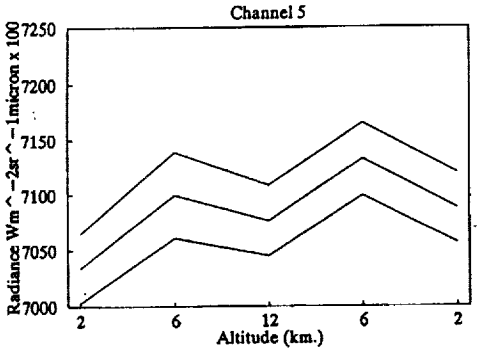

Variation of Ch#5 radiance at sensor with altitude.

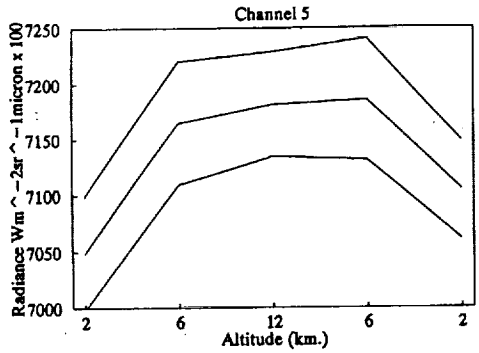

Variation of Ch#5 upwelling ground radiance with altitude.

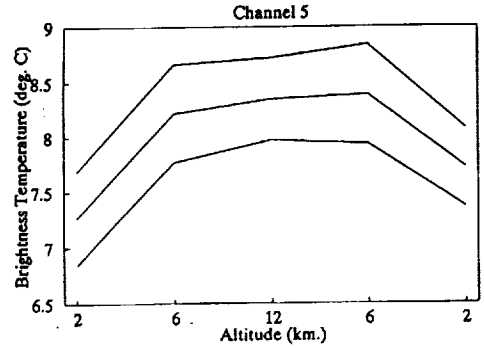

Variation of Ch#5 Brightness Temperature with altitude.

ANALYSIS OF TIMS PERFORMANCE SUBJECTED TO SIMULATED WIND BLAST.

S. Jaggi S. Kuo

Lockheed Engineering & Sciences Company
Stennis Space Center, MS 39529

Summary

This report describes the results of the performance of the TIMS when it is subjected to various wind conditions in the laboratory. Various wind conditions were simulated using a 24" fan or combinations of air jet streams blowing toward either or both of the blackbody surfaces. The fan was used to simulate a large volume of air flow at moderate speeds (up to 30 mph). The small diameter air jets were used to probe TIMS system response in reaction to localized wind perturbations. The maximum nozzle speed of the air jet was 60 mph. A range of wind directions and speeds were set up in the laboratory during the test. The majority of the wind tests were conducted under ambient conditions with the room temperature fluctuating no more than 2 °C. The temperature of the high speed air jet was determined to be within 1 °C of the room temperature. TIMS response was recorded on analog tape. Additional thermistor readouts of the blackbody temperatures and thermocouple readout of the ambient temperature were recorded manually to be compared with the housekeeping data recorded on the tape. Additional tests were conducted under conditions of elevated and cooled room temperatures. The room temperature was varied between 19.5 to 25.5 °C in these tests.

The calibration parameters needed for quantitative analysis of TIMS data were first plotted on a scanline-by-scanline basis. These parameters are the low and high blackbody temperature readings as recorded by the TIMS and their corresponding digitized count values. Using these values, the system transfer equations were calculated. This equation allows us to compute the flux for any video count by computing the slope and intercept of the straight line that relates the flux to the digital count. The actual video of the target (the lab floor in this case) was then compared with a simulated target. This simulated target was assumed to be a blackbody at emissivity of °.95 and the temperature was assumed to be at ambient temperature as recorded by the TIMS for each scanline. Using the slope and the intercept the flux corresponding to this target was converted into digital counts. The counts were observed to have a strong correlation with the actual video as recorded by the TIMS.

The attached graphs describe the performance of the TIMS when compressed air is blown at each one of the blackbodies at different speeds. The effect of blowing a fan and changing the room temperature is also being analyzed. Results indicate that the TIMS system responds to variation in wind speed in real time and maintains the capability to produce accurate temperatures on a scan line basis.

TIMS wind analysis – Ch#2 Calibration parameters
Compressed air towards high BB

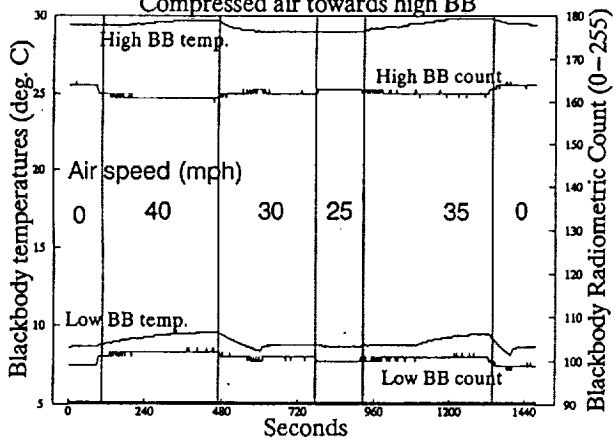

TIMS wind analysis – Ch#2 System Transfer Equation
Compressed air towards low BB

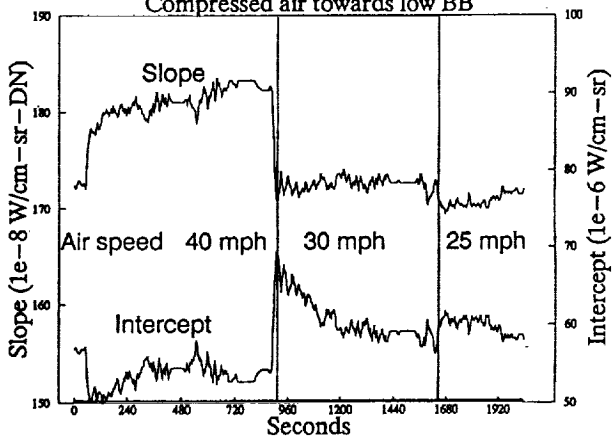

TIMS wind analysis – Ch#2 Actual & Predicted Video
Compressed air towards high BB

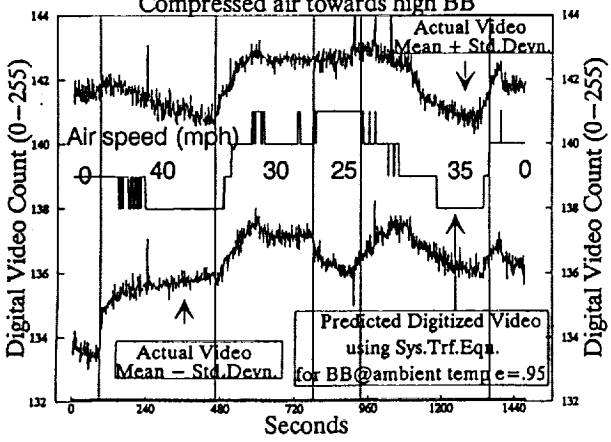

TIMS wind analysis – Ch#2 Calibration parameters
Compressed air towards low BB

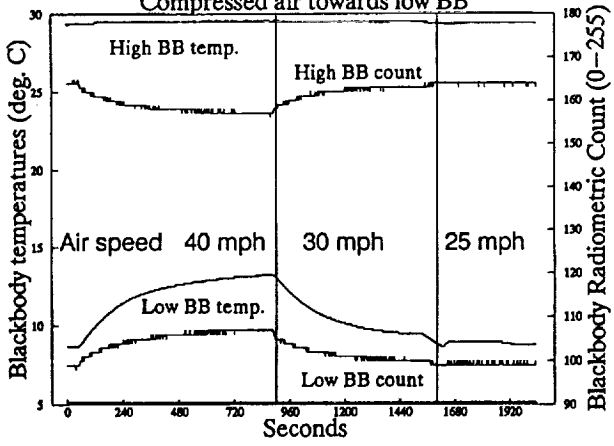

TIMS wind analysis – Ch#2 System Transfer Equation
Compressed air towards high BB

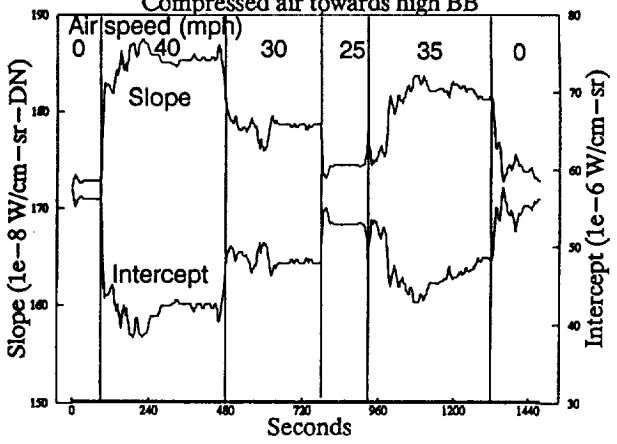

TIMS wind analysis – Ch#2 Actual & Predicted Video
Compressed air towards low BB

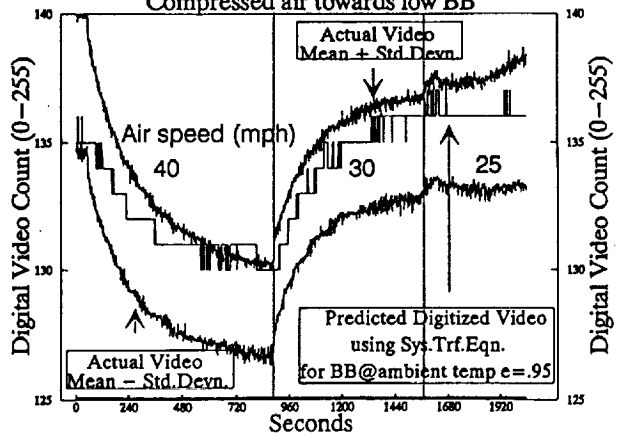

54-43
189099
P 3

N94-16599

SENSITIVITY OF BLACKBODY REFERENCE PANELS TO WIND BLAST

Gordon Hoover
Jet Propulsion Laboratory
4800 Oak Grove Drive, Pasadena, California 91109

As part of the effort at Stennis and JPL to discover the root causes of TIMS' temperature calibration errors, we undertook a series of experiments to measure the sensitivity of a heated plate to cooling by wind blast.

We set up a powerful blower which was capable of generating a jet of wind in excess of 200 miles per hour. In the jet we mounted an electrically heated copper plate, one quarter of an inch thick and six inches square. The electrical heaters were capable of delivering a total power of 800 watts. The power to the heaters was feedback controlled with reference to a thermistor mounted on the back of the copper plate. The plate was mounted about 2.5 feet from the blower nozzle, at about 45 degrees to the direction of the jet. The jet was wide enough to wash the whole surface and its temperature at the plate was about 28 C.

In order to simulate temperature differences which approximated flight conditions, we ran the plate at about 65 C, for a delta T of 37 C.

The plate was instrumented with thermocouples in an attempt to measure the strength of temperature gradients within the plate. We placed thermocouples in holes drilled into the edge of the plate, in holes drilled from face to face, and surface mounted with a clamp. We found it quite difficult to measure the plate temperature in a way that we felt was insensitive to errors caused by the wind. For instance, merely clamping the thermocouple junction bead onto the surface with a small fiberglass tab led to errors of over five degrees due to heat flowing into the wind-cooled thermocouple leads.

We observed apparent lateral gradients as well as depth gradients, but in the most extreme cases, the temperature differences within the copper metal amounted to no more than 1.0 C.

If one considers the area covered by one of the 100 watt heater elements, one can easily calculate the

maximum gradient that can be sustained with the heater at maximum output power. The power density was 5.2 watts per square centimeter. The handbook value for the conductivity of copper was 3.8 watts/cm*degree(C). After some calculating, I arrive at the maximum delta T of 0.82 C.

1) delta T = Power*thickness/(area*conductivity)

Since full output power was not required to maintain the 37 C temperature difference, the maximum delta T inside the plate must be less than this estimate, maybe even as low as 0.1 or 0.2 C.

The next step was to measure the gradient across the paint layer. Since paint has a much lower conductivity than copper, maybe it could sustain a gradient large enough to account for the errors. Two techniques were attempted.

Method 1

Method 1 required the comparison of the radiance of the wind blown target to a reference target unaffected by the wind. For this second target we used a sheet metal horn immersed in a stirred hot water bath. The temperature of the water was adjusted to approximate the anticipated temperature of the interior of the plate by reference to thermocouples fixed to the immersed horn and imbedded in the plate. The blower and plate heater were then turned on and the plate was allowed to reach a steady state.

At this point, brightness temperatures were measured for the target and the comparison horn with a Barnes PRT5 Precision Radiation Thermometer and with an Omega radiation thermometer.

As confirmation of the accuracy of the comparison, measurements were made of the two targets after the blower had been turned off and the plate had reached its new steady state. Under these conditions, the gradients through the plate and paint are minimized. The difference in brightness temperature between the plate and the immersed horn under these conditions are entirely due to the actual plate-horn difference and to the possible non-unity of the plate emissivity.

Method 2

The paint used on the heated copper plate was presumed to account for the greater part of the temperature drop during the operation of the blower. It is relatively easy to calculate the expected effect from increasing the thickness of the paint and to argue backwards to derive a conductivity for the paint from a

comparison of the brightness temperature of two patches of different thickness.

Thickened paint patches two centimeters square were applied with multiple coats to areas of the plate which had been nearly isothermal in prior observations. The thicknesses were measured with a depth micrometer.

The plate and the blower were then turned on and allowed to reach a steady state. The brightness temperature across the plates was observed using an Inframetrics Model 520 Thermal Camera and images were recorded on video tape. The Inframetrics camera is equipped with the ability to display the temperature profile generated by a single scan line. The sweep across the unequal patches of paint showed the brightness temperature differences clearly and this information permitted the temperature drop across the paint layer.

Once the conductivity was known, we were able to calculate the temperature drop to be expected across a single thin layer of paint. This value could then be compared with the temperature drop from method 1.

One thing we discovered in the course of our experiments was that the single thickness coat of paint that appeared to eye to be solid black, fell short of being a perfect blackbody. The emissivity was estimated by a a number of methods, as follows:

Under conditions of no wind, with the plate heated to a steady state, the brightness temperature of the surface was compared to the temperature of the interior of the plate. The gradient across the paint was assumed to be zero, attributing the whole drop observed to the departure of the plate from blackness. The radiance observed under these conditions is the sum of the thermally emitted radiation and the reflected radiation from the surroundings where the experiment was being conducted. We took this latter temperature to be the ambient air temperature.

2) Total Radiance = emissivity * BB(T plate)
+ (1 - emissivity) * BB(T air)

$$\text{2a) emissivity} = \frac{(\text{total rad.} - BB(T_{air})}{(BB(T_{plate}) - BB(T_{air}))}$$

In these formulas, the simplified form for the reflected term which derives partially from Kirchhoff's Law was adopted in the absence of detailed knowledge of the angular dependence of the incident radiation and the reflectivity of the plate.

COMPARISON OF PRELIMINARY RESULTS FROM AIRBORNE ASTER SIMULATOR(AAS) WITH TIMS DATA

Yoshiaki Kannari, Franklin Mills, Hiroshi Watanabe, Teruya Ezaka, Tatsuhiko Narita, and *Sheng-Huei Chang
JAPEX Geoscience Institute, Inc.
Akasaka Twin Tower, East Wing Third Floor,2-17-22,Akasaka, Minato-ku,Tokyo, Japan
* Geophysical Environmental Research Corp.
1 Bennett Common Millbrook, New York 12545

1.INTRODUCTION

The Japanese Advanced Spaceborne Thermal Emission and Reflection radiometer(ASTER), being developed for a NASA EOS-A satelite, will have 3 VNIR, 6 SWIR, and 5 TIR (8-12um) bands. An Airborne ASTER Simulator(AAS) has been developed for Japan Resources Observation System Organization (JAROS) by the Geophysical Environmental Research(GER) Corp. to research surface temperature and emission features in the MWIR/TIR, to simulate ASTER's TIR bands, and to study further possibility of MWIR/TIR bands.

ASTER Simulator has 1 VNIR, 3 MWIR (3-5um), and 20 (currently 24) TIR bands. We collected data over 3 sites -- Cuprite, Nevada; Long Valley/Mono Lake,California; and Death Valley, California --with simultaneous ground truth measurements. We present preliminary data collected by AAS for Cuprite, Nevada and compare AAS data with TIMS data.

2.AIRBORNE ASTER SIMULATOR DATA

The AAS data were acquired during the afternoon of Dec.5,1991. Each image is 495 lines of 544 pixels(512 data, 16 heated reference black body, 16 ambient reference blackbody). Each pixel is signed 15 bit data. Table 1 lists the approximate center wavelength and full-width at half- maximum(FWHM) for each channel based on preliminary laboratory tests. Additional information on the AAS can be found in Watanabe,et.al.(1991). The raw AAS data was converted to radiance by using the following equation:

$$Rad_d = (DN_d - DN_w)/(DN_c - DN_w)*(Rad_c - Rad_w) + Rad_w$$

The radiances for each reference blackbody were calculated based on the temperatures recorded by the operator at the beginning of each image and the center wavelength of the nominal bandpasses. The temperatures of the black bodies were assumed constant for the entire image. DN_w was determined, separately for each scan line, by averaging the DN values of the heated blackbody on that

scan line. DN_c was determined in a similar manner for the ambient black body. After conversion to radiances, the radiances were converted to 8-bit integers and processed to create panchromatic, false color, and decorrelation stretch images. The normalization method was used to determine temperature and emissivity for each pixel and channel.

Performance data for AAS were estimated from approximate spectral tests at NASA Stennis Space Center and laboratory test at GER. Performance was also estimated by the Cuprite data which has good outcrops of quartzite, opalized rocks and carbonate rocks.

3.COMPARISON OF AAS DATA WITH TIMS DATA

TIMS data for the western Cuptite were acquired on Sept.1,1990. This TIMS data covered the same area of AAS CPWA2 data. The performances of TIMS were well known.

Comparison of decorrelation stretch images from TIMS data with those of AAS data shows that the TIMS image of band 1·3·4 is similar to a part of the AAS image of band 2·5·6 or band 2·4·6 or band 2·5·7 for 4 selected sites (Figure 1).

The decorrelation stretch images from the AAS are not as clean as the TIMS decorrelation images. This is caused by several factors. First, the TIMS data was collected over much higher ground temperatures. Second, the bandwidths of the AAS are narrower than TIMS for most channels. Third, the decorrelation stretch amplifies the noise level in an image.

This comparison provides some spectral performances and band characteristics of the current AAS .

4.CONCLUSION

Estimated center wavelengths of the AAS in its Dec. 1991 configuration are listed in table 1. The FWHM bandwidth for the Dec. 1991 AAS was 0.2-0.6μm, varying with channel. The Dec. 1991 FWHM for most channels is narrower than TIMS. Accordingly, the S/N ratio of the Dec. 1991 AAS field survey data is less than TIMS Sept. 1990 field survey data. The Dec. 1991 AAS NEdT, estimated from field survey data, is about 0.3-1.0K in the TIR bands.

Following approximate calibration measurements at SSC in April 1992, GER will adjust and modify the AAS to improve its performance before the Sept. 1992 data collections.

ACKNOWLEDGEMENTS

We would like to thank Mr.G.Hoover, Ms.C.Grove, and Mr.N.Biery for their cooperation in fieldwork. We would also thank JAROS for support of this work.

REFERENCE

R.P.Ashley and M.J.Abrams, Alteration Mapping using multispectral images -

Cuprite mining district, Esmeralda county,Nevada, USGS Open-File Report, 1980, 80-367

H.Watanabe, M.Sano, F.Mills, S.H.Chang, and S.Masuda,Airborne and Spaceborne thermal multispectral remote sensing,Proc. of SPIE Conference,Vol.1490 -34,1991

Table 1. Estimated Characteristics Of AAS For Dec. 1991 Survey Flight.

Channel	Detector System	Estimated Center Wavelength(Dec.91)	Estimated FWHM(Dec.91)
1	TIR1	----	-----
2	TIR1	8.2	0.6
3	TIR1	8.6	0.5
4	TIR1	8.9	0.5
5	TIR1	9.3	0.3
6	TIR1	9.6	0.25
7	TIR1	9.8	0.2
8	TIR1	9.9	0.25
9	TIR1	10.3	0.2
10	TIR1	10.5	0.2
11	TIR1	10.7	0.2
12	TIR1	----	----
13	TIR2	----	----
14	TIR2	9.8	0.2
15	TIR2	9.9	0.2
16	TIR2	10.1	0.2
17	TIR2	10.3	0.2
18	TIR2	10.5	0.2
19	TIR2	10.7	0.2
20	TIR2	11.0	0.4
21	TIR2	----	---
22	TIR2	11.5	0.3
23	TIR2	----	---
24	TIR2	----	---
25	MWIR	3.0-3.6	
26	MWIR	3.6-4.2	
27	MWIR	4.4-5.0	
28	VNIR	0.75-0.85	

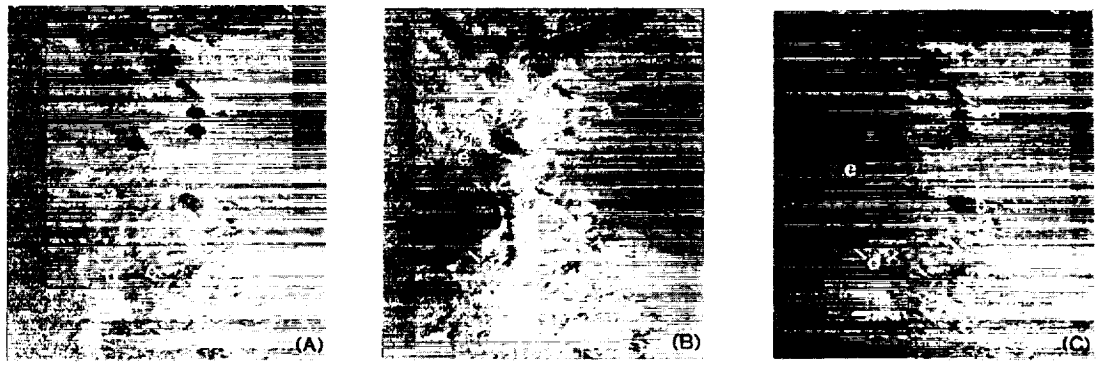

Figure 1. Decorrelation Stretch Image of TIMS Band 134 and Those Images of AAS. (A) Band 256 (B) Band 246 (C) Band 257

APPLICATION OF SPLIT WINDOW TECHNIQUE TO TIMS DATA

Tsuneo Matsunaga, Shuichi Rokugawa, and Yoshinori Ishii

Department of Mineral Development Engineering,
Faculty of Engineering, University of Tokyo
7-3-1, Bunkyo-ku, Tokyo, 113, Japan

1. INTRODUCTION

Absorptions by the atmosphere in thermal infrared region are mainly due to water vapor, carbon dioxide, and ozone. As the content of water vapor in the atmosphere greatly changes according to weather conditions, it is important to know its amount between the sensor and the ground for atmospheric corrections of TIMS data (i.e. radiosonde). On the other hand, various atmospheric correction techniques have already been developed for sea surface temperature estimations from satellites. Among such techniques, Split Window technique, now widely used for AVHRR(Advanced Very High Resolution Radiometer), uses no radiosonde or any kind of supplementary data but a difference between observed brightness temperatures in two channels for estimating atmospheric effects.

In this paper, applications of Split Window technique to TIMS data are discussed because availability of atmospheric profile data is not clear when ASTER operates. After these theoretical discussions, the technique is experimentally applied to TIMS data at three ground targets and results are compared with atmospherically corrected data using LOWTRAN7 with radiosonde data.

2. SPLIT WINDOW TECHNIQUE

The theory of Split Window technique is based on equations of radiative transfer at two different wavelengths(for a detailed theory, see *McMillin et al. 1984*). To eliminate atmospheric terms from these equations, several approximations and assumptions(surface emissivities in two channels are unity, atmospheric absorptions are small and so on) are introduced, and equation (1) is derived:

$$T_1 - T_2 = \frac{k_2 - k_1}{k_1}(T_s - T_1) \tag{1}$$

where T_1 and T_2 are observed brightness temperatures in channel 1 and 2, T_s is surface brightness temperature, and k_1 and k_2 are absorption coefficients in channel 1 and 2. Equation (1) shows that the difference between surface and observed temperatures(T_s -T_1) is proportional to the difference between observed temperatures in different channels(T_1 -T_2).

A coefficient of (T_s -T_1) is usually determined by linear regressions of computer-simulated data(*Deschamps et al. 1980*) or buoy and satellite data set(*Strong et al. 1984*). In this aspect, this technique is an empirical one. As a result, a constant value is added to (1) because of approximation errors and (1) becomes equation (2).

$$T_s = T_1 + a(T_1 - T_2) + b \quad \text{or} \quad T_s = a_1 T_1 + a_2 T_2 + b \tag{2}$$

3. TIMS CHANNEL COMBINATIONS FOR SPLIT WINDOW TECHNIQUE

To determine suitable channel combinations of TIMS for Split Window technique, brightness temperatures observed in TIMS channels were calculated using LOWTRAN7 for six model atmospheres, three surface temperatures for each model atmospheres, two looking angles(nadir and 45°), and the airplane altitude 4km. Results are shown in Fig. 1a and Fig. 1b. Linear relationships between temperatures are almost satisfied for TIMS channel 5 and 6 combination(5/6), and combination 1/3. Non-linearities for combination 1/5, 3/4, and 4/5 probably come from differences between model atmospheres and atmospheric ozone. These figures suggest combinations 1/3 and 5/6 are best combinations for Split Window technique.

4. ESTIMATION OF LAND/WATER SURFACE TEMPERATURE USING TIMS DATA

TIMS data used in this study were acquired over the Jasper Ridge area(between San Francisco and San Jose, California), at 11:30 a.m., August 30, 1990. Surface radiation temperatures were simultaneously measured at three locations(Searsville Lake, rubber running track, and asphalt parking lot) and a radiosonde was launched from near the lake. TIMS data were converted into radiance and brightness temperature using internal reference data(air blast effects on reference surface temperature were corrected according to *Schmugge et al. 1990*). Radiance values were atmospherically corrected using LOWTRAN7 with radiosonde data and converted into brightness temperatures at the ground level.

Coefficients of equation (2) were determined by LOWTRAN7 simulations. In this case, five relative humidity profiles based on Mid Latitude Summer model were used in the simulations instead of six model atmospheres. Simulation results are shown in Fig. 2, and coefficients were determined as follows (subscripts indicate TIMS channel):

$$T_s=T_3+1.705(T_3-T_1)-0.94 \quad \text{and} \quad T_s=T_5+3.238(T_5-T_6)+0.03 \quad (3)$$

Results of temperature estimations are shown in Table1. Temperatures atmospherically corrected with Mid Latitude Summer model are higher than with radiosonde data because the model overestimates the amount of water vapor. Estimated temperatures using Split Window technique agree with temperatures atmospherically corrected with radiosonde data within 2°C for Searsville Lake and the running track. But for the parking lot, the discrepancy is relatively large probably because of spectral variations of the surface emissivity.

5. CONCLUSION

Split Window technique can be applied to TIMS data if the channel combination is suitable. But equation (3) may not be used for other cases because coefficients of equation (2) depend on the type of the atmosphere and the altitude of the airplane.

Acknowledgments

We would like to thank Dr. A. B. Kahle for giving a permission to use TIMS data, and Dr. C. D. Elvidge, Dr. S. J. Hook, G. Hoover, Z. Yu, Dr. H. Watanabe, and Y. Kannari for their field works and helpful discussions.

Reference

1) Schmugge, T., M. Stoll, and T. Phulpin, TIMS observation in HAPEX, Proceedings of the Second TIMS Workshop, JPL Publ. 90-55, 49-56, 1990.
2) Deschamps, P. Y., and T. Phulpin, Atmospheric correction of infrared measurements of sea surface temperature using channels at 3.7, 11 and 12 μm, Boundary-Layer Meteorology, 18, 131-143,1980.

3) Strong, A. E., and E. P. McMillin, Improved ocean surface temperatures from space - Comparisons with drifting buoys, Bulletin American Meteorological Society, 65, 2, 138-142, 1984.
4) McMillin, L. M., and D. S. Crosby, Theory and validation of the multiple window sea surface temperature technique, Journal of Geophysical Research, 89, C3, 3655-3661, 1984.

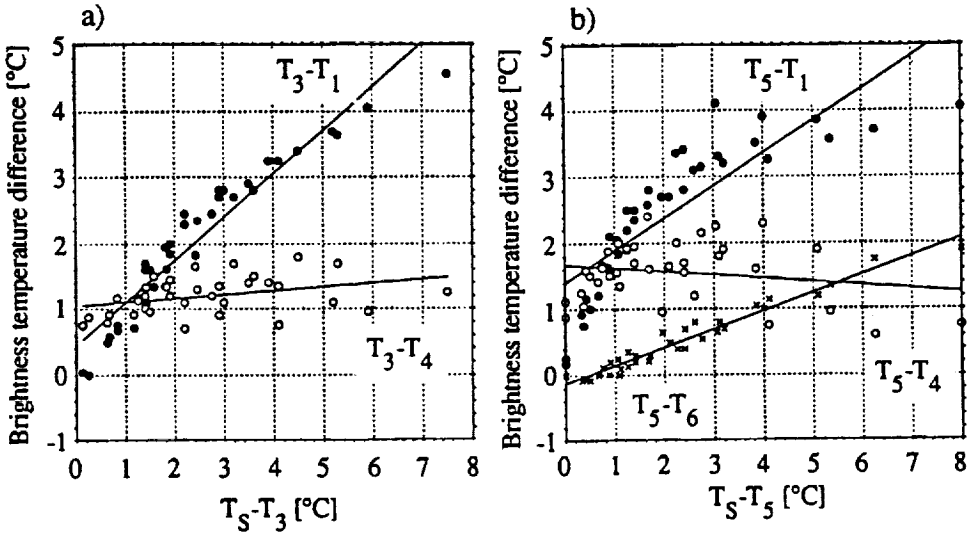

Fig. 1. Results of LOWTRAN7 simulations: T_S is surface brightness temperature and T_1,T_3,T_4,T_5 and T_6 are remotely observed brightness temperatures in TIMS Ch. 1, 3, 4, 5 and 6, respectively.

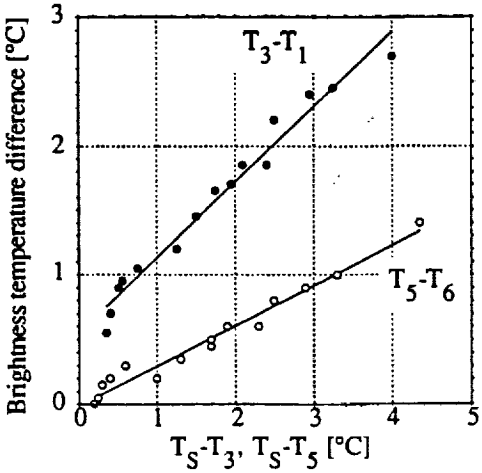

Fig. 2. Results of LOWTRAN7 simulations using five relative humidity profiles for TIMS Jasper Ridge data.

Table 1. Surface Temperature Estimation using Split Window Technique

[°C]	Lake	Track	Lot
TIMS observed			
average	18.9	40.7	31.7
(low)	(17.6)	(37.3)	(29.6)
(high)	(19.6)	(42.3)	(33.1)
Ch. 3 - Ch. 1	1.6	5.0	2.0
Ch. 5 - Ch. 6	0.6	1.8	-0.1
Ground Truth	22.0	48.0	38.0
Midlat. Summer			
average	21.6	51.7	39.6
(low)	(21.2)	(50.5)	(37.3)
(high)	(22.0)	(53.4)	(43.3)
Radiosonde			
average	20.6	48.2	36.8
(low)	(20.3)	(47.8)	(35.6)
(high)	(20.9)	(48.6)	(39.1)
Split Window			
Ch.1 and 3	21.0	49.9	34.1
Ch. 5 and 6	21.3	47.9	32.6

ATMOSPHERIC CORRECTIONS FOR TIMS ESTIMATED EMITTANCE

T. A. Warner and D. W. Levandowski

Earth and Atmospheric Sciences
Purdue University
West Lafayette, Indiana 47907-1397

Figure 1 shows the estimated temperature of the average of 500 lines of TIMS data of the Pacific Ocean, from flight line 94, collected on September 30, 1988, at 1931 GMT. In Figure 1A, with no atmospheric corrections, estimated temperature decreases away from nadir (the center of the scan line). In Figure 1B, a LOWTRAN modeled correction (Kneizys, *et al.*, 1985), using local radiosonde data and instrument scan angle information, results in reversed limb darkening effects for most bands, and does not adequately correct all bands to the same temperature. The atmosphere tends to re-radiate energy at the wavelengths at which it most absorbs, and thus the overall difference between corrected and uncorrected temperatures is approximately 4^{0} C, despite the average LOWTRAN calculated transmittance of only 60% between 8.1 and 11.6 μm. An alternative approach to atmospheric correction is a black body normalization. This is done by calculating a normalization factor for each pixel position and wavelength, which when applied to Figure 1A, results in a single calculated temperature, as would be expected for a gray body with near uniform emittance.

The black body adjustment is based on the atmospheric conditions over the sea. Figure 2 shows the ground elevation profile along the remaining 3520 scan lines (approximately 10 km) of flight line 94, up the slopes of Kilauea, determined from aircraft pressure and laser altimeter data. This flight line includes a large amount of vegetation that is clearly discernible on the radiance image, being much cooler than the surrounding rocks. For each of the 3520 scan lines, pixels were classified as vegetation or "other" (see Figure 3). A moving average of 51 lines was applied to the composite vegetation emittance (Warner and Levandowski, 1990) for each scan line, to reduce noise (Figure 4). Assuming vegetation to be like water, and to act as gray body with an emittance of 0.986 across the spectrum, Figure 4A shows that the LOWTRAN induced artifacts are severe, and other than for the 0.9.9 μm channel, not significantly different from applying no corrections at all. As expected, with increasing elevation atmospheric effects are slightly reduced (Figure 4B), because moisture tends to be concentrated in the lowermost part of the atmosphere. The black body adjustment (Figure 4C) is highly robust, and even at elevations nearly 600 meters above the sea, remains an alternative procedure for use in calculating emittance.

ACKNOWLEDGMENTS

Special thanks to Haluk Cetin, Elsa Abbott, Vince Realmuto and Anne Kahle for their help. This research was partially supported by the I.M.M.R.R.I. (U.S. Bureau of Mines grant G1114118), as well as by a 1992 Purdue University A. H. Ismail Interdisciplinary Program Doctoral Research Award.

REFERENCES

Kneizys, F. X., E. P. Shettle, W. O. Gallery, J. H. Chetwyn, L. W. Abreu, J. E. A. Selby, S. A. Clough, and R. W. Fenn 1985, *Atmospheric Transmittance / Radiance: Computer Code LOWTRAN 6*, Optical Physics Division, Project 7670, Air Force Geophysical Laboratory, Hanscom AFB.

Warner, T. A. and D. W. Levandowski, 1990. Optimum Band Selections for Estimating Emittance from TIMS Data. In: Abbott, E. A. (Ed.) *Proceedings of the second Thermal Infrared Multispectral Scanner (TIMS) workshop, June 6, 1990.* JPL Publication 90-55: 26-30.

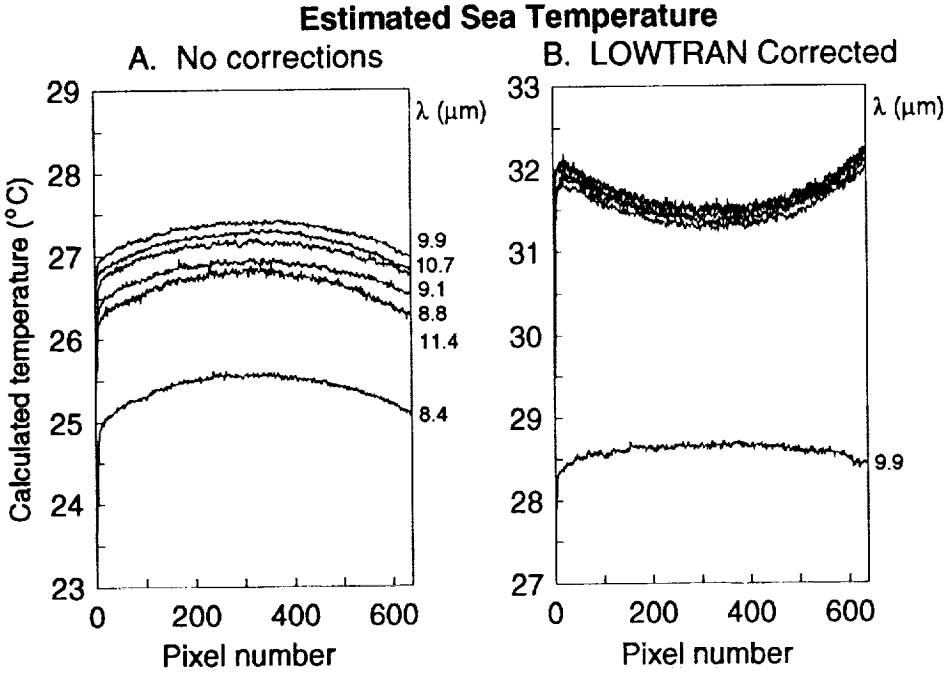

Figure 1. Radiance data from the average of 500 lines of TIMS data of the Pacific Ocean, converted to estimated black body temperatures. A. Temperatures esitmated with no atmospheric corrections. B. Temperatures estimated using LOWTRAN modelled atmospheric parameters.

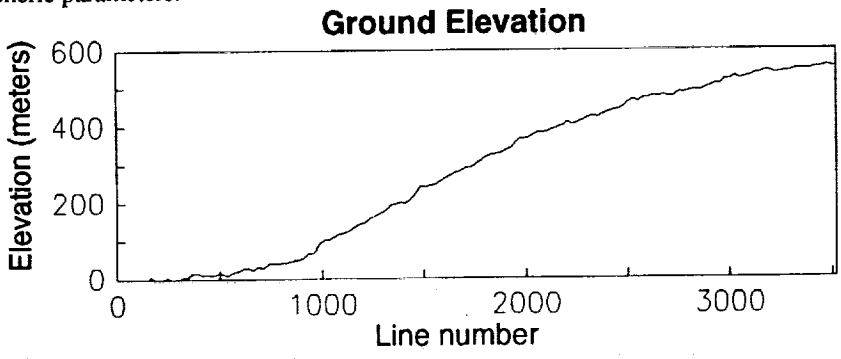

Figure 2. Nadir ground elevation for part of TIMS flightline 94, estimated from laser and pressure altimeter data.

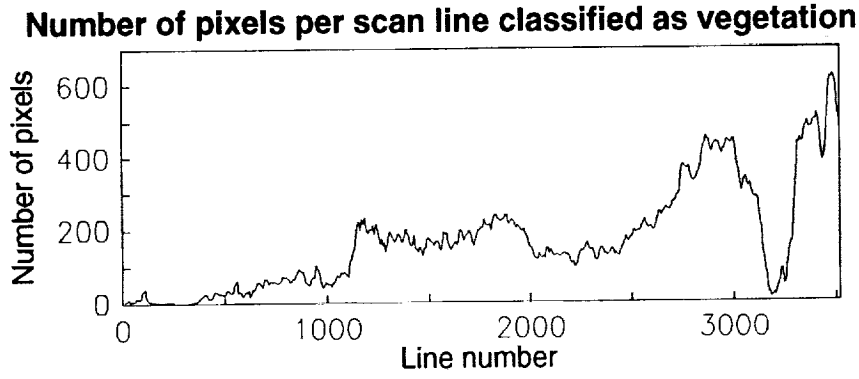

Figure 3. Number of pixels in each scan line classified as vegetation.

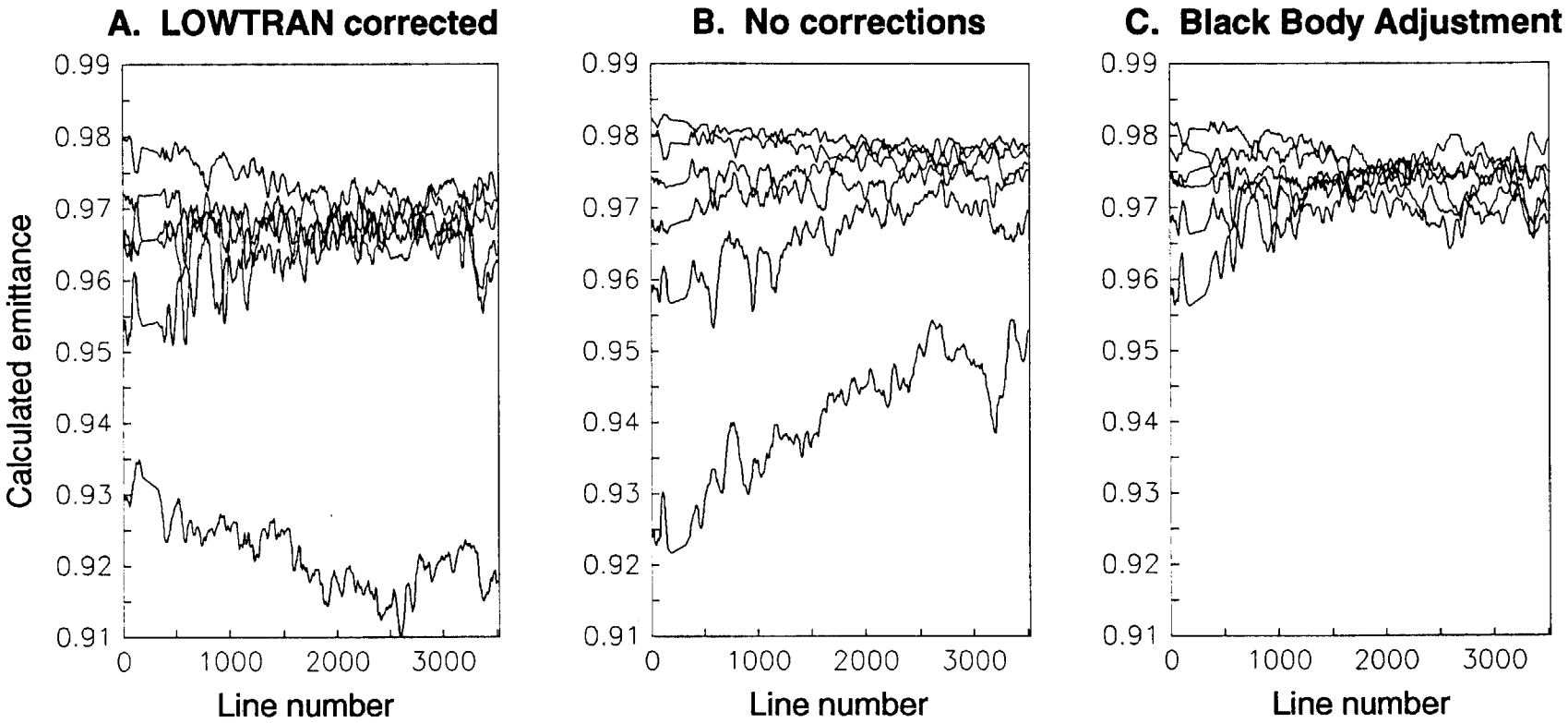

Figure 4. Calculated six band emmitance for vegetation versus scan line number. Ground elevation increases with increasing line number (see Figure 2.) A. Lowtran corrected (Lowermost curve is 9.9 μm). B. No corrections applied. (Lowermost curve is 8.4 μm.) C. Black body adjustment.

58-43
189103
P. 3

N94-16603

AN ALGORITHM FOR THE ESTIMATION OF BOUNDS ON THE EMISSIVITY AND TEMPERATURES FROM THERMAL MULTISPECTRAL AIRBORNE REMOTELY SENSED DATA

S. Jaggi

Lockheed, Stennis Space Center Mississippi 39529

D. Quattrochi

NASA, Stennis Space Center, Mississippi 39529

R. Baskin

U.S. Geological Survey, Salt Lake City, Utah 84104

The effective flux incident upon the detectors of a thermal sensor, after it has been corrected for atmospheric effects, is a function of a non-linear combination of the emissivity of the target for that channel and the temperature of the target. The sensor system cannot separate the contribution from the emissivity and the temperature that constitute the flux value.

In this paper, we describe a method that estimates the bounds on these temperatures and emissivities from thermal data. This method is then tested with remotely sensed data obtained from NASA's Thermal Infrared Multispectral Scanner (TIMS) - a 6 channel thermal sensor. Since this is an under-determined set of equations i.e there are 7 unknowns (6 emissivities and 1 temperature) and 6 equations (corresponding to the 6 channel fluxes), there exist theoretically an infinite combination of values of emissivities and temperature that can satisfy these equations. Using some realistic bounds on the emissivities , bounds on the temperature are calculated. These bounds on the temperature are refined to estimate a tighter bound on the emissivity of the source. An error analysis is also carried out to quantitatively determine the extent of uncertainty introduced in the estimate of these parameters. This method is useful only when a realistic set of bounds can be obtained for the emissivities of the data. In the case of water the lower and upper bounds were set at 0.97 and 1.00 respectively.

Five flights were flown in succession at altitudes of 2 km (low), 6 km (mid), 12 km (high), and then back again at 6 km and 2 km. The area selected was the Ross Barnett reservoir near Jackson, Mississippi. The mission was flown during the predawn hours of Feb. 1, 1992. Radiosonde data was collected for that duration to profile the characteristics of the atmosphere. Ground truth temperatures using thermometers and radiometers were also obtained over an area of the reservoir. The results of two independent runs of the radiometer data averaged 7.03±.70 for the first run and 7.31±.88 for the second run.

The results of the algorithm yield a temperature of 7.68 for the low altitude data to 8.73 for the high altitude data.

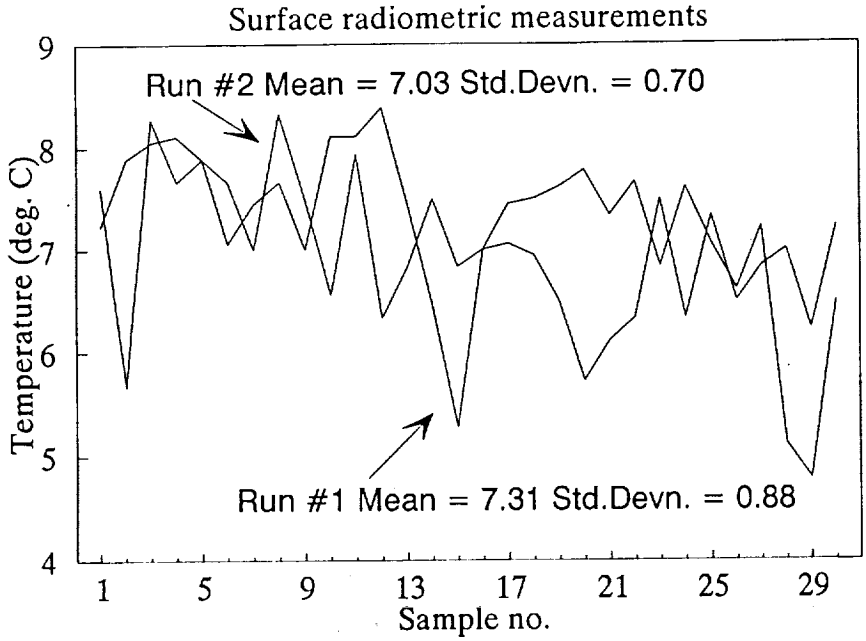

Distribution of reservoir surface temperature 5AM 2/1/92

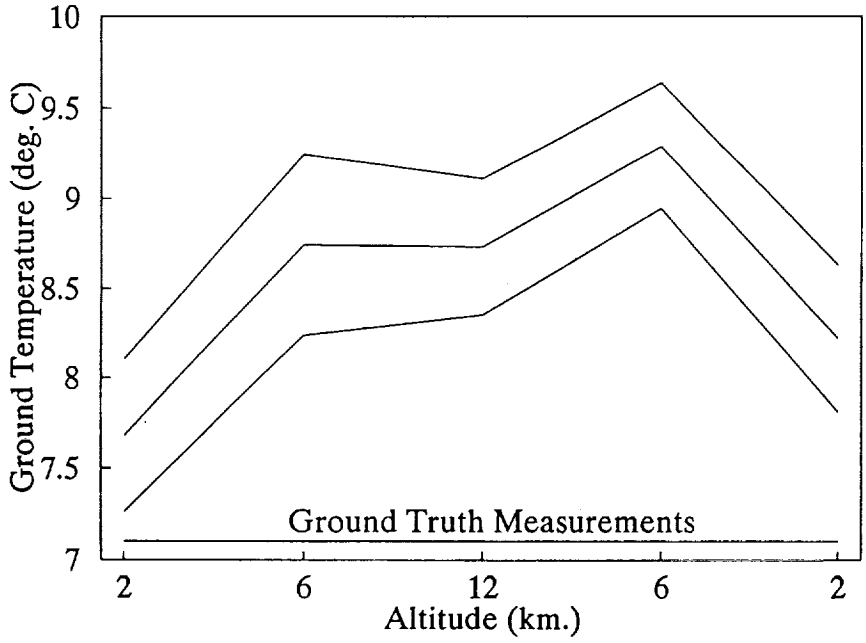

Variation of Ground Temperature with altitude.

Average of brightness temperature in all channels.

Flt.Ln.	Mean	Sigma	Mean-sigma	Mean+Sigma
1	6.51	0.306	6.204	6.816
2	7.45	0.278	7.172	7.728
3	7.86	0.234	7.626	8.094
4	8.38	0.282	8.098	8.662
5	7.39	0.321	7.069	7.711

Groung temperature using the bounds algorithm.

Flt. Ln.	Mean	Sigma	Mean-sigma	Mean+Sigma
1	7.68	0.422	7.258	8.102
2	8.74	0.504	8.236	9.244
3	8.73	0.380	8.350	9.110
4	9.29	0.348	8.942	9.638
5	8.22	0.410	7.811	8.630

MULTI-RESOLUTION PROCESSING FOR FRACTAL ANALYSIS OF AIRBORNE REMOTELY SENSED DATA

S. Jaggi

Lockheed,Stennis Space Center, Mississippi 39529

D. Quattrochi

NASA, Stennis Space Center, Mississippi 39529

N. Lam

Louisiana State University, Baton Rouge, Louisiana 70803

Fractal geometry is increasingly becoming a useful tool for modeling natural phenomenon. As an alternative to Euclidean concepts, fractals allow for a more accurate representation of the nature of complexity in natural boundaries and surfaces. Since they are characterized by self-similarity, an ideal fractal surface is scale-independent; i.e at different scales a fractal surface looks the same. This is not exactly true for natural surfaces. When viewed at different spatial resolutions parts of natural surfaces look alike in a statistical manner and only for a limited range of scales.

In this paper, images acquired by NASA's Thermal Infrared Multispectral Scanner are used to compute the fractal dimension as a function of spatial resolution. Three methods are used to determine the fractal dimension - Shelberg's line-divider method, the variogram method and the triangular prism method. A description of these methods and the result of applying these methods to a remotely-sensed image is also presented.

Five flights were flown in succession at altitudes of 2 km (low), 6 km (mid), 12 km (high), and then back again at 6 km and 2 km. The area selected was the Ross Barnett reservoir near Jackson, Mississippi. The mission was flown during the predawn hours of Feb. 1, 1992. Radiosonde data was collected for that duration to profile the characteristics of the atmosphere. This corresponds to 3 different pixel sizes - 5m , 15m and 30m. After, simulating different spatial sampling intervals within the same image for each of the 3 image sets, the results are cross-correlated to compare the extent of detail and complexity that is obtained when data is taken at lower spatial intervals.

Introduction

The advent of fractal analysis measures has been alluded to as one of the four most significant scientific concepts of the 20th century, with a scientific impact similar to that created by quantum mechanics, the general theory of relativity, and the development of the double-helix model in DNA structure. (Clarke et al. 1991) Since the development of the fractal concept by Mandelbrot (Mandelbrot 1967, Mandelbrot 1977), a number of methods for calculating fractal dimensions have been developed and applied to various spatial problems. (Goodchild 1980, Goodchild 1982, Burrough 1981, Mark et al. 1984, Goodchild et al. 1987, Krummel et al. 1987, Milne 1991, Lam et al. 1992) Fractals, however, have seen only limited employment for analysis of remote sensing data. (DeCola 1989, Lam 1990) As noted in Lam (1990), fractals offers significant potential

for improvement of measurement and analysis of spatially and spectrally complex remote sensing images. The fractal dimension of remote sensing data could yield quantitative insight on the spatial complexity and information content. Thus, remote sensing data acquired from different sensors and at differing spatial and spectral resolutions could be compared and evaluated based on fractal measurements. The fractal dimensions derived from remote sensing data could also be compared with other measures of spatial complexity to better understand the significance of the spatial interrelationships present within image data. Moreover, if fractal dimensions are shown to be unique to different types of remote sensing data, these values could be used as control for the simulation of fractal surface generation of remotely sensed images.

Outside of the potential offered by fractal analysis, the only other method for measuring the spatial frequency as an index of variability and complexity within a remote sensing image has been the two-dimensional Fourier transform technique (2D-FFT). In spite of being computationally intensive, the 2D-FFT technique has been successfully used for spatial processing of image data, such as filtering. (Moik 1980) The only information that a 2D-FFT can provide to classify data in a spatial manner is the spectrum of the data. For example, urban areas have a higher spatial frequency than rural areas. The information is very qualitative and does not readily lend itself to quantitative interpretation. With the emergence of fractals, it may be possible to lend that quantitative analysis of these spatial variations.

This paper describes the adaptation and implementation of three methods that have been successfully applied to compute fractal dimensions from multiple scaled remote sensing data. These are the Shelberg or line-divider method, (Shelberg et al. 1982, Shelberg et al. 1983) the triangular prism method, (Clarke et al. 1991), and the variogram method. (Mark et al. 1984) These techniques have been implemented on a self-contained menu-driven PC-compatible image interpretation software package (Note: This package is also available for the UNIX workstation environment, without the menu structure, as a set of routines). This interactive program, written in 'C', allows the user to analyze their results without having to spend considerable effort in programming these methods for fractal computation. The results are accessible to the user on the screen as well as from an ASCII file for future use in graphing and more intensive interpretation. Also, this PC-compatible software utilizes almost no special purpose hardware (except for a VGA monitor), which permits wide distribution to other users.

On entering the program, the user encounters an image on the screen with a menu adjacent to it. The menu allows the user to perform analyses using either of the three fractal computation methods. The fractal dimension is computed for a user-specified region within the image. This region is outlined as a rectangular box on the image. The user can then interactively move the box anywhere or change the size of the box. Also, some of these methods allow for analysis to be performed using different values for specific internal parameters. These parameters can also be changed interactively or can be preset by the user. The following is a discussion of the three fractal computation methods, their implementation using the program, and a description of the results obtained from each fractal calculation method.

Reference

Burrough P.A., 1981. Fractal dimension of landscapes and other environmental data. *Nature*, 294(19):240-42.

Clarke K.C. and Schweizer D. M., 1991. Measuring the fractal dimension of natural surfaces using a robust fractal estimator. Cartography and Geographic Information Systems, 18(1):37-47.

DeCola L., 1989. Fractal analysis of a classified Landsat scene. *Photogrammetric Engineering and Remote Sensing*, 55(5):601-610.

Goodchild M.D., 1982. The fractional Brownian process as a terrain simulation model. *Modeling and Simulation*, 13:1133-1137.

Goodchild M.F., 1980. Fractals and the accuracy of geographical measures. *Mathematical Geology*, 12:85-98.

Goodchild M.F. and D.M. Mark, 1987. The fractal nature of geographic phenomena. *Annals of the Association of American Geographers*, 77(2):265-78.

Krummel J.R., Gardner R.H., Sugihara G., O'Neill R.V. and Coleman P.R., 1987.*Oikos*, 48:321-24.

Lam N.S-N and Quattrochi D.A, 1992. On the issues of scale, resolution, and fractal analysis in the mapping sciences. *The Professional Geographer*, 44(1):88-98.

Lam N.S-N, 1990. Description and measurement of Landsat TM images using fractals. *Photogrammetric Engineering and Remote Sensing*, 56(2):187-195.

Mandelbrot B.B., 1967. How long is the coast of Britain? Statistical self-similarity and fractional dimension. *Science*, 156:636-638.

Mandelbrot B.B., 1977. *Fractals: Form, Chance and Dimension*. San Francisco: Freeman.

Mark D.M. and P.B. Aronson, 1984. Scale-dependent fractal dimensions of topographic surfaces: An empirical investigation, with applications in geomorphology and computer mapping. Mathematical Geology 16(7):671-683.

Milne B.T. 1991. Lessons from applying fractal models to landscape patterns. *In Quantitative Methods in Landscape Ecology*, ed. M.G. Turner and R.H. Gardner, 199-235. New York: Springer-Verlag.

Moik J.G., 1980. *Digital Processing of Remotely Sensed Images*. NASA SP-431. Washington, D.C.: National Aeronautics and Space Administration.

Shelberg M.C., H. Moellering and N. S-N. Lam, 1982. Measuring the fractal dimensions of empirical cartographic curves. Proceedings, Fifth International Symposium on Computer-Assisted Cartography (Auto-Carto 5), Washington, D.C.: 481-490.

Shelberg M.C., Lam N. S-N., and Moellering H., 1983. Measuring the fractal dimensions of surfaces. Proceedings, Sixth International Symposium on Automated Cartography (Auto-Carto 6), Ottawa, Ontario, Canada, 2:319-328.

PRELIMINARY ANALYSIS OF THERMAL-INFRARED MULTISPECTRAL SCANNER DATA OF THE IRON HILL, COLORADO CARBONATITE-ALKALIC ROCK COMPLEX

by
Lawrence C. Rowan[1], Kenneth Watson[2], Susanne H. Miller[2]
[1] U.S. Geological Survey - MS 927 Reston, VA 22092
[2] U.S. Geological Survey - MS 964 Denver, CO 80225

1. GEOLOGIC SETTING

The Iron Hill carbonatite-alkalic igneous rock complex is in the Powderhorn mining district, approximately 40 km south-southwest of Gunnison, Colorado . The complex, which occupies about 30 km^2, was emplaced in metasedimentary and metavolcanic rocks during the late Precambrian or early Cambrian (Olson and Hedlund, 1981). The main rock types in the complex, from oldest to youngest, are fenite, pyroxenite, uncompahgrite, ijolite, nepheline syenite, and dolomitic carbonatite. The carbonatite is limonitic and forms an elliptically shaped 4km^2 stock. Calcitic and dolomitic carbonatite dikes are also numerous throughout the complex and in the pre-existing rocks. Pyroxenite is the most widespread rock type within the complex, but pyroxene is extensively altered to biotite, phlogopite, and vermiculite. Fenite, which formed through Na, K-metasomatism of the country rocks (Heinrich, 1980), typically contains more feldspar and less quartz than the equivalent unaltered country rocks. The other alkalic rock types are less widespread and less well exposed. Parts of the complex are covered by Oligocene ash-flow tuff and alluvial, colluvial, and glacial deposits. Sagebrush and grass cover is moderately dense to very dense at low to intermediate elevations; coniferous tree cover is dense at high elevations and on some north-facing slopes at lower elevations.

2. DATA PROCESSING

TIMS data were acquired of the Iron Hill area on July 22, 1990 from a mean altitude above terrain of 4000m. Weather conditions prior to the flight indicated that the ground was dry. Initial data calibration was conducted by assuming a linear relationship between the observed blackbody signals and the band pass fluxes at the hot and cold blackbody temperatures convolved with the spectral responses for the six channels (Palluconi and Meeks, 1985). The coefficients of this linear relationship were then used to convert the observed signals to equivalent fluxes. A generic spectral atmospheric correction for the path radiance, transmission, and downward sky radiance based on MODTRAN (Berk et al., 1989) was then employed.

Several methods have been used for extracting spectral emissivity information from TIMS data (Gillespie et al., 1986; Kahle and Rowan, 1980; Lahren et al., 1988; Watson and Raines, 1989; Watson et al., 1990; Gillespie, 1986; Hook et al., 1990; Kealy and Gabell, 1990). Decorrelation stretches have been commonly used (Gillespie et al., 1986), although they are of limited value because they do not yield interpretable spectral information.

In this study a new algorithm (Watson, 1992a) is used to compute spectral emissivity ratios, independent of any emissivity assumptions. This algorithm has the advantage that any of the possible emissivity ratios can be computed and, thus, a large variety of composite ratio images can be constructed, which permits examination of various geologic hypotheses based on the spectral properties of the surface materials.

Prior to processing the TIMS data, evaluation of laboratory reflectance spectra of field samples identified 13 TIMS ratios that might be useful for distinguishing the main rock types.

Initial analysis of these ratio images resulted in selection of the following images for detailed evaluation: $^{2}/_{1}$, $^{3}/_{1}$, $^{4}/_{1}$, $^{5}/_{1}$, $^{1}/_{6}$, $^{3}/_{6}$, and $^{2}/_{5}$. A vegetation mask, which was based on high $^{3}/_{2}$ digital numbers, was used to reduce the influence of vegetation on the contrast stretches and, hence, increase lithologic discrimination. The cause of the high digital numbers in vegetated areas in this and the other ratio images is not clear. The ratio images were then spatially filtered to remove scanline noise using a two-dimensional fast-Fourier transformation (Watson, 1992b) and registered to a 1:24,000 topographic map. The registration was accomplished by first using a small set of control points to perform an affine transformation and, then, an inverse distance weighed algorithm (Hummer-Miller, 1990) was employed using over 100 control points.

3. INTERPRETATION AND CONCLUSIONS

Most of the alkalic igneous rocks (pyroxenite, ijolite, and uncompahgrite) are readily distinguished from the silica-saturated rocks (quartzite, granite, and ash-flow tuff)in each of several color-ratio composite images, especially those including the $^{2}/_{1}$, $^{5}/_{1}$, $^{1}/_{6}$, $^{3}/_{6}$, and $^{3}/_{1}$ ratios. This implied large spectral emissivity contrast is consistent with the markedly different laboratory reflectance spectra of these two rock groups. In general, quartzite, granite, and ash-flow tuff are spatially separable in the color-ratio composite images, but color variations within the alkalic-rock group may reflect the proportions of rock, soil, and vegetation, as well as rock composition differences. Although the carbonatite stock is distinctive from the alkalic rocks, it is difficult to distinguish from some of the other rock types.

Distinction of the carbonatite from tuff and from some granitic areas, and separation of the fenite from granite were only feasible using color-ratio composite images which had had the vegetation mask applied prior to contrast stretching. Several different masked color-ratio composite images were needed to display subtle spectral emissivity difference that are critical for mapping these lithologic variations. Discrimination of the carbonatite is hampered by the location of the weak CO_3 reststrahlen feature between TIMS channels 5 and 6.

4. REFERENCES

Berk, A., Bernstein, L.W., and Robertson, D.C., 1989, A moderate resolution model for LOWTRAN 7: Geophys. Lab., Air Force Systems Command, Hanscom Air Force Base, MA, GL-TR-89-0122.

Gillespie, A.R., 1986, Lithologic mapping of silicate rocks using TIMS: The TIMS Data User's Workshop June 18 and 19, 1985, NSTL Miss., JPL Publ. 86-38, p. 29-44.

Gillespie, A.R.,Kahle, A.B., and Walker, R.E., 1986, Color enhancement of highly correlated images.I. Decorrelation and HSI contrast stretches: Remote Sens. of Env., v. 20, p. 209-235.

Heinrich, E.W., 1980, The geology of carbonatites: Huntington, New York, Robert E. Krieger Pub. Co., 585 p.

Hummer-Miller, S., 1990, Techniques for noise removal and registration of TIMS data: Photo. Engr. and Rem. Sens., v. 56, n. 1, p. 49-53.

Hook, S.J., Gabell, A.R., Green, Kealy, P.S., and Kahle, A.B., 1990, A comparison of the model emittance, thermal log residual and alpha residual techniques using TIMS data acquired over Cuprite, Nevada: Proc. Second TIMS Workshop, JPL Publ. 90-55, p. 17-25.

Kahle, A.B., and Rowan,L.C., 1980, Evaluation of multispectral middle infrared aircraft images for lithologic mapping in the East Tintic Mountains, Utah: Geology, v. 8, p. 234-239.

Kealy, P.S., and Gabell,A.R., 1990, Estimation of emissivity and temperature using alpha coefficients: Proc. Second TIMS Workshop, June 1990, JPL Publ. 90-55, p. 11-16.

Lahren, M.M., Schweickert, and Taranik, J.V., 1988, Analysis of the northern Sierra accreted terrane, California, with airborne thermal infrared multispectral scanner data: Geology, v. 16, p. 525-528.

Olson, J.C., and Hedlund, D.C., 1981, Alkalic rocks and resources of thorium and associated elements in the Powderhorn districts, Gunnison County, Colorado: U.S. Geol. Survey Prof. Paper 261, p. 75.

Palluconi, F.D., and Meeks, G.R., 1985, Thermal Infrared Multispectral Scanner (TIMS): An investigator's guide to TIMS data: Jet Propulsion Lab. Publ. 85-32.

Watson, K., 1992a, Spectral ratio method for measuring emissivity; in press, Jour. Rem. Sens. Env.
Watson, K., 1992b, Image processing using the two-dimensional Fast Fourier Transform - noise reduction and other appliçation: submitted to Geophysics.
Watson, K. and Raines, G.L., 1989, Exploration remote sensing - a look to the future: in Proc. of Exploration '87, Third Decennial Int. Conf. on Geophy. and Geochm. Expl. for Minerals and Groundwater, ed. G.D. Garland, Ont. Geol. Surv., sp. vol.3, p. 78-87.
Watson, K., Kruse, F.A., and Hummer-Miller, S., 1990, Thermal infrared exploration in the Carlin trend, northern Nevada: Geophysics, v.55, n.1., p. 70-79.

THE USE OF TIMS FOR MAPPING DIFFERENT PAHOEHOE SURFACES: MAUNA IKI, KILAUEA

Scott K. Rowland

Planetary Geosciences, Dept. of Geology & Geophysics
2525 Correa Rd. Honolulu, Hawaii 96822

INTRODUCTION

S-type and p-type pahoehoe record different mechanisms and vigors of activity within an active flow field (e.g. Swanson 1973; Hon 1991; Multhaup & Walker 1992). There is some controversy about what these mechanisms are exactly, and this study was undertaken with the idea that an accurate map of the two surfaces within a pahoehoe flow field could be helpful in solving the problem. TIMS allows discrimination between s-type and p-type pahoehoe, and this ability has been used to map the two surface types on the Mauna Iki satellitic shield (southwest rift zone, Kilauea Volcano).

TIMS has previously been used to discriminate a'a from pahoehoe as well as to determine relative age relationships of different flows (e.g. Kahle *et al.* 1988; Abrams *et al.* 1991). Although inter-flow variation was minor in the data published by these authors, a second goal of the work presented here is to understand such variations to better constrain intra-flow differences used for age dating.

DATA USED

The TIMS data were collected in November 1985 and have a spatial resolution of ~10 m. An image consisting of the first 3 principal components (PC) and detailed field checking were used to derive a unit map (Figure 1). The PC image was useful for unit discrimination but because we found that the spectral character of the two pahoehoe surface types changed downflow, no rigorous classification scheme was devised.

After constructing the unit map, we extracted broad-band TIMS spectra to aid in explaining the mechanism behind the ability to discriminate the two lava types. We also made measurements of surface temperature in the field using a thermocouple. Quantitative analysis of the PC image, the spectra, and the surface temperature measurements (in collaboration with colleagues at JPL) is ongoing.

S-TYPE AND P-TYPE PAHOEHOE

S-type and p-type pahoehoe differ both in their character and their distributions within a flow field. In short, s-type pahoehoe is vesicle-rich (s stands for spongy), and is erupted directly from a lava tube. The surface of s-type consists of stretched and broken vesicles, and often spalls off shortly after emplacement. P-type pahoehoe is vesicle poor, and its chilled margin resembles obsidian. The reason for the paucity of vesicles comprises the present controversy. The most commonly-held idea is that p-type pahoehoe resides within a flow field for a period of time long enough to degas. If that particular storage area is then invaded by fresher lava, the degassed lava is pushed out on to the surface. This explains the transition from early p-type to later s-type lava often seen while watching a lava breakout. A large amount of degassing is known to

take place during flow in tubes (also recently investigated using TIMS: Realmuto *et al.* 1991).

The competing idea is that p-type pahoehoe is actually richer in gas than s-type, and the pressure provided by the overlying flow field in which it resides causes solution of gas back into the lava. P-type pahoehoe often has a lower aspect ratio, possibly reflecting a lower viscosity generated by the higher dissolved gas content. Arguing against this is the fact that reabsorbtion of gas is endothermic whereas p-type pahoehoe is often hotter than s-type upon eruption.

S-TYPE AND P-TYPE DISTRIBUTION AT MAUNA IKI

In Figure 1, the "main shield" and "downrift flow" were determined by field mapping and studying the eruption chronology. Within these two zones, the distribution and relative amounts of s-type and p-type pahoehoe differ greatly. On the main shield, p-type pahoehoe is restricted to 3 small patches along the northwest margin of the flow. It is here that lava flows from the Mauna Iki summit ponded against pre-existing topography. This is a condition conducive to stagnation of the flow and consequent inflation. The p-type pahoehoe erupted out of storage within this stagnated flow. The major activity on the main shield was the overflowing of relatively gas-rich lava from a small lava pond, and the formation of p-type pahoehoe was an exception.

The downrift flow was emplaced by lava tubes, and the distribution and relative abundance of the two pahoehoe types are very different. They make up roughly equal proportions of the flow and at contacts p-type overlies s-type. Overall, the Mauna Iki eruption had a low eruption rate, and this was particularly true of the final lava tube stage. This low eruption rate meant that once the flow field was established, it was difficult to supply all of it with fresh lava.

The distribution of p-type pahoehoe on the flow field can be used to constrain the conditions required for formation. First, there is a paucity of p-type pahoehoe where lava tubes were well-established (i.e. on the shield and the main axis of the downrift flow). This indicates that initially, lava erupted directly from tubes was too gas-rich to form p-type. The downrift flow field averages ~1 m in thickness, and is even thinner along its margins. The large amount of p-type pahoehoe compared to the flow volume as a whole argues against the existence of an overburden capable of pressurizing the lava. The field relations suggest instead, that even though gas-rich lava established the distal end of the flow initially, in the waning later stages all the lava degassed during sluggish travel down the tubes prior to being erupted onto the surface.

Kipukas (inliers) of s-type tumuli form semi-linear trains branching off from the main axis of the downrift flow. These may indicate the lines of subsidiary early-formed tubes, and the ability to map tubes long after a lava flow has stopped erupting would be a very useful tool. We are in the process of conducting this same type of analysis on the Mauna Ulu flow field where the positions of lava tubes were closely monitored during the eruption.

FUTURE WORK AND CONCLUSIONS

The TIMS data indicate that at Mauna Iki the radiometric temperature of s-type pahoehoe is hotter than that of p-type, supported by the fact that PC1 discriminates the two types most strongly. Further analysis of the TIMS data, as well as more complete field temperature measurements,will help to determine if these differences are due to

different physical temperatures or emissivities. In conclusion, it is possible to discriminate pahoehoe surface types using TIMS data. Quantitative analyses of the causative relationships, however, have not been completed, and these are the next goals. With regard to the formation of p-type pahoehoe, the large area covered by p-type, including areas where the flow as a whole is thin, suggests that the availability of an overburden is not required for its formation, in turn supporting the degassed origin.

I am very grateful to Harold Garbeil for helpful discussions and for his image processing skills.

REFERENCES

Abrams M, Abbot E, & Kahle A (1991). Combined use of visible, reflected infrared, and thermal infrared images for mapping Hawaiian lava flows. J. Geophys. Res. **96**: 475-484.

Hon K & Kauahikaua J (1991). The importance of inflation in formation of pahoehoe sheet flows. EOS **72**: 557.

Kahle AB, Gillespie AR, Abbot EA, Abrams MJ, Walker RE, Hoover G, & Lockwood JP (1988). Relative dating of Hawaiian lava flows using multispectral thermal infrared images: a new tool for geologic mapping of young volcanic terranes. J. Geophys. Res. **93**: 15,239-15,251.

Multhaup RA & Walker GPL (1992). P and S-type pahoehoe: a study of vesicle distribution patterns in Hawaiian lava flows. J. Volcanol. Geotherm. Res. (in press).

Realmuto VJ, Hon KA, & Kahle AB (1991). Mapping lava tubes, age relationships, and silicified regions in the Kuapaianaha lava field with multispectral thermal infrared remote sensing. EOS **72**: 557.

Swanson DA (1973). Pahoehoe flows from the 1969-1971 Mauna Ulu eruption, Kilauea volcano, Hawaii. G.S.A. Bull. **84**: 615-626.

Figure 1. Unit map derived from TIMS data for the Mauna Iki flow.

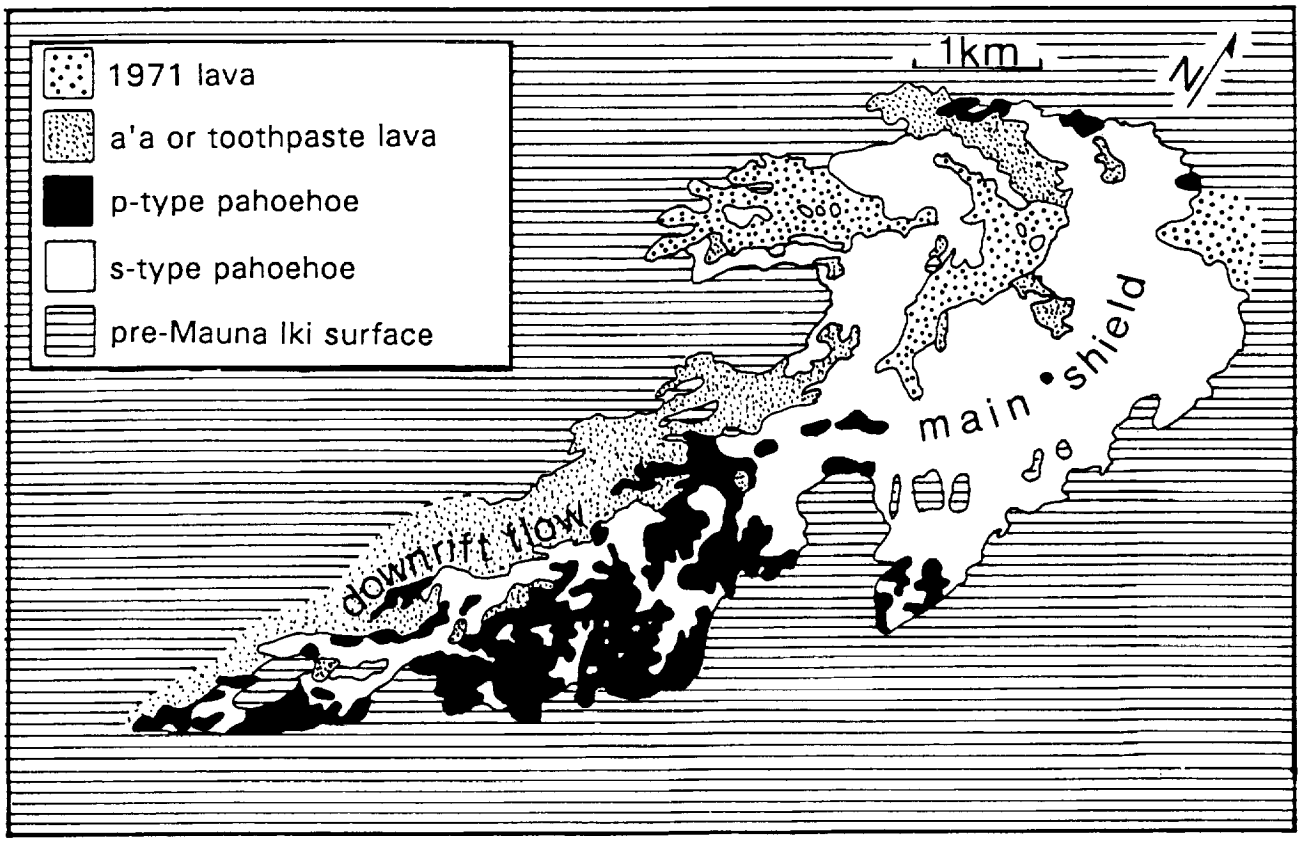

EJECTA PATTERNS OF METEOR CRATER, ARIZONA DERIVED FROM THE LINEAR UN-MIXING OF TIMS DATA AND LABORATORY THERMAL EMISSION SPECTRA

Michael S. Ramsey and Philip R. Christensen

Department of Geology, Arizona State University
Tempe, Arizona 85287-1404

1. INTRODUCTION

Accurate interpretation of thermal infrared data depends upon the understanding and removal of complicating effects. These effects may include physical mixing of various mineralogies and particle sizes, atmospheric absorption and emission, surficial coatings, geometry effects and differential surface temperatures. The focus of this study is the examination of the linear spectral mixing of individual mineral or endmember spectra. Linear addition of spectra, for particles larger than the wavelength *(Salisbury et al, 1987)*, allows for a straight-forward method of deconvolving the observed spectra, predicting a volume percent of each endmember. The 'forward analysis' of linear mixing (comparing the spectra of physical mixtures to numerical mixtures) has received much attention *(Thomson & Salisbury 1991; Christensen et al, 1986)*. The reverse approach of un-mixing thermal emission spectra has been examined with remotely sensed data *(Adams et al, 1989; Gillespie et al, 1990)*, but no laboratory verification exists. Understanding of the effects of spectral mixing on high resolution laboratory spectra allows for the extrapolation to lower resolution, and often more complicated, remotely gathered data.

Thermal Infrared Multispectral Scanner (TIMS) data for Meteor Crater, Arizona were acquired in September, 1987. The spectral un-mixing of these data gives a unique test of the laboratory results. Meteor Crater (1.2 km in diameter and 180 m deep) is located in north-central Arizona, west of Canyon Diablo *(Shoemaker & Kieffer, 1974)*. The arid environment, paucity of vegetation and low relief make the region ideal for remote data acquisition. Within the horizontal sedimentary sequence that forms the upper Colorado Plateau, the oldest unit sampled by the impact crater was the Permian Coconino Sandstone. A thin bed of the Toroweap Formation, also of Permian age, conformably overlays the Coconino. Above the Toroweap lies the Permian Kiabab Limestone which, in turn, is covered by a thin veneer of the Moenkopi Formation. The Moenkopi is Triassic in age and has two distinct sub-units in the vicinity of the crater. The lower, Wupatki member, is a fine-grained sandstone, while the upper, Moqui member, is a fissile siltstone *(Shoemaker & Kieffer, 1974)*. Ejecta from these units are preserved as inverted stratigraphy up to 2 crater radii from the rim. The mineralogical contrast between the units, relative lack of post-emplacement erosion *(Grant & Schultz, 1989)* and ejecta mixing provide a unique site to apply the un-mixing model. Selection of the aforementioned units as endmembers reveals distinct patterns in the ejecta of the crater.

2. LABORATORY SPECTRA

Particles between 355 and 500μm were used to reduce the effects of volume scattering; the choice of endmember minerals approximates the mixing of Kiabab Limestone and Coconino Sandstone in the crater ejecta. Laboratory thermal emission spectra (Fig. 1) of the powders were acquired on a Mattson Cygnus 100 FTIR interferometer/spectrometer. Absolute emissivity was obtained using the technique described by *(Christensen & Harrison, 1992)*. The endmember components, mixed by volume into binary mixtures, were agitated after each of the five spectral acquisitions. This process assured accurate spectral sampling and charted the daily variation of the spectrometer, which varied by less than 1% absolute emissivity. The five runs were then averaged to produce a final spectrum. The calcite endmember spectra shows the characteristic absorption band associated with the vibration of the carbonate ion (≈1550 cm^{-1}) and the large reststrahlen band produced by the Si-O bending mode of quartz (≈1150 cm^{-1}) *(Salisbury et al, 1987)*.

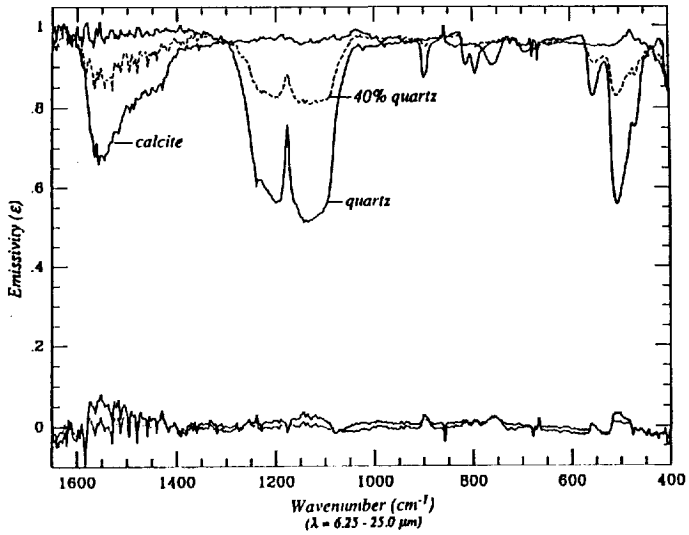

FIG. 1. Emission spectra of 355-500μm quartz and calcite. The dashed line shows the physical mixture of 40% quartz, 60% calcite. Errors (Δε) in the model fit for the 40% quartz mixture are shown in the bottom curves. The solid line is the two endmember case, while the dotted line indicates the improved error after blackbody correction.

The spectra of the two endmembers were used as reference inputs to the model. A least-squares fit of the data results in the percentage of each endmember as well as the "goodness-of-fit" of the model to the data (rms error) *(Adams et al, 1989; Gillespie et al, 1990)*. Figure 2 shows the results for the quartz endmember. Predicted percentages were within 8% of actual values and validate the linear assumption for particles larger than the wavelength. The largest rms errors (Fig. 1) occur over the strong absorption features, and are due to a band shallowing in the spectra of the physical mixtures. The behavior over these regions, a function of the photon path length and the imaginary part of the index of refraction k(λ), appears to be slightly non-linear. The use of unimodal grain sizes virtually eliminates a change in the path length, indicating the non-linear behavior must be related to the change in the overall k(λ) of the mixture. The band shallowing can be approximated by the addition of blackbody emissivity *(Ramsey & Christensen, 1992)*.

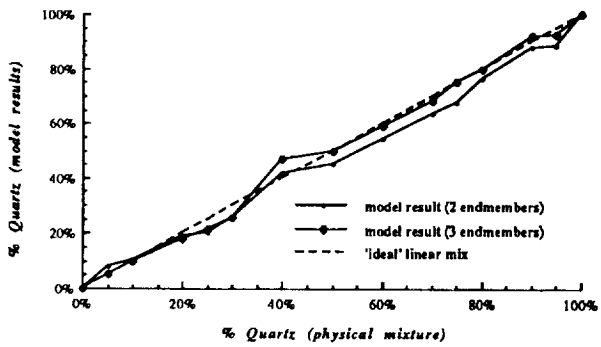

FIG. 2. Model predicted results for the percentage of quartz. Squares indicate the values obtained using two endmembers; the diamonds show the improved results using blackbody emissivity as a third endmember.

Using a constant emissivity of 1.0 as a third endmember improved the results to better than *5%*, reducing the errors over the bands. The model, re-run on the lab spectra convolved to TIMS resolution, predicted the percentages to within *10%*; however, no attempt was made to model the effect of additional noise.

3. METEOR CRATER IMAGE ANALYSIS

Standard image enhancement techniques such as the decorrelation stretch do not account for large temperature differentials within the scene and tend to stretch microphonic noise as well. A spectral un-mixing analysis eliminates these problems, however. For this study, six emissivity images were extracted from the TIMS data using the spectrum normalization technique *(Realmuto, 1990)*. An improvement in the algorithm allows for interactive linear stretching of the emissivity images for a maximum spectral contrast prior to input into the un-mixing program. The aforementioned stratigraphic units were used as endmembers for the model (5 total). These endmembers accurately fit the data to within ± 2 DN except for areas over the buildings and road. The Coconino endmember image clearly reveals a NE trending windstreak *(Grant & Schultz, 1989)*, which is a thin (<50 cm) veneer of eolian-derived material. In addition, subtle patterns within the Kiabab indicate the true extent of the ejecta. This supports the interpretation of *(Grant & Schultz, 1989)* who state that the ejecta is well-preserved below the thin alluvial mantling deposits derived from Holocene erosion. These patterns are not evident in the decorrelation stretched image and must be field verified. Differentiation of slight mineralogical changes within the Moenkopi are also clearly distinguished and allow for improved eject mapping.

4. REFERENCES

Adams, J.B., M.O. Smith, and A.R. Gillespie, Simple models for complex natural surfaces: a strategy for the hyperspectral era of remote sensing, in *Proc. IEEE Intl. Geosci. & Remote Sensing Symp.*, 16-21, 1989.

Christensen, P.R., H.H. Kieffer, S.C. Chase, D.D. Laporte, A thermal emission spectrometer for identification of surface composition from earth orbit, in *Commercial applications and scientific research requirements for thermal infrared observations of terrestrial surfaces, NASA-EOSAT Joint Report*, 119-132, 1986.

Christensen, P.R. and S.T. Harrison, Thermal-infrared emission spectroscopy of natural surfaces: application to desert varnish coatings on rocks, to be submitted to - *J. Geophys. Res.*, 1992.

Gillespie, A.R., M.O. Smith, J.B. Adams and S.C. Willis, Spectral mixture analysis of multispectral thermal infrared images, in *Abbott, E.A. (Ed.), Proc. of the Second TIMS Workshop, JPL Pub. 90-55*, JPL, Pasadena, Calif., 57- 74, 1990.

Grant, J.A. and P.H. Schultz, The erosional state and style of Meteor Crater, Arizona, *Lunar and Planet. Sci. XX*, 355-356, 1989.

Ramsey, M.S. and P.R. Christensen, The linear "un-mixing" of laboratory infrared spectra: implications for the thermal infrared emission spectrometer (TES) experiment, Mars Observer, *Lunar and Planet. Sci. XXIII*, 1127-1128, 1992.

Realmuto, V.J., Separating the effects of temperature and emissivity: emissivity spectrum normalization, in *Abbott, E.A. (Ed.), Proc. of the Second TIMS Workshop, JPL Pub. 90-55*, JPL, Pasadena, Calif., 26-30, 1990.

Salisbury, J.W., B. Hapke, and J.W. Eastes, Usefulness of weak bands in the midinfrared remote sensing of particulate planetary surfaces, *J. Geophys. Res. 92*, 702-710, 1987.

Shoemaker, E.M. and S.E. Kieffer, Guidebook to the geology of Meteor Crater, Arizona: *ASU Center for Meteorite Studies Publication 17*, Tempe, Arizona, 66p, 1974.

Thomson, J.W. and J.W. Salisbury, The mid-infrared reflectance of mineral mixtures (7-14 μm), submitted - *Remote Sensing of the Enviro.*, 1991.

THE USE OF TIMS DATA TO ESTIMATE THE SO_2 CONCENTRATIONS OF VOLCANIC PLUMES: A CASE STUDY AT MOUNT ETNA, SICILY

Vincent J. Realmuto

Jet Propulsion Laboratory
California Institute of Technology

MS 183-501, 4800 Oak Grove Drive, Pasadena, California 91109

TIMS data were acquired over Mount Etna, Sicily, on July 29, 1986 (Bianchi et al. 1990). The volcanic activity at that time was characterized by the steady effusion of gas from the Bocca Nuova (BN), Chasm, and Southeast craters. The Northeast crater, quiet at the time of the TIMS overflight, was the site of Strombolian eruptive activity between July 31 and September 24, 1986 (SEAN 1986).

In aerial photographs of the Etna summit region acquired during the TIMS overflight, the SO_2-rich plume is visible due to the scattering of sunlight by the entrained aerosols. In the TIMS imagery, the plume is revealed by the strong absorption of SO_2 between 8 and 9 μm. This absorption feature falls within the first three channels of TIMS, with the strongest absorption falling within Channel 2. Following decorrelation processing, the plume is visible in color-composites of TIMS channels 2, 3, and 5.

To estimate the concentration of SO_2 within the plume, the LOWTRAN 7 radiative transfer code was used to model to radiance spectra measured by TIMS. Inputs to LOWTRAN included ground temperature and emissivity, vertical profiles of atmospheric temperature and humidity, and the vertical position of SO_2 within the plume. The ground temperatures and emissivity spectra were derived from the TIMS measurements through the use of a curve-fitting algorithm (Warner and Levandowski 1990, Realmuto 1990). Emissivity spectra recovered outside of the plume were applied to the ground beneath the plume where appropriate. The ground temperature estimates were modified interactively by fitting LOWTRAN-generated radiance values to those measured in TIMS channels 4, 5, and 6, the channels that were not strongly affected by the presence of SO_2 in the atmosphere. The atmospheric pressure, temperature, and humidity profiles were recorded by radiosondes launched from Trapani, which is located approximately 220 km west of Mount Etna.

To evaluate the accuracy and precision of the estimation procedure, SO_2 concentrations were recovered over the same piece of ground using the data from three successive TIMS overflights. The flights were separated by intervals of approximately 15 minutes. Assuming that the gas output of the volcano was constant during the course of the flights, the concentration of SO_2 in the chosen portion of the plume was 26.3 ± 4.1 mg/m^3. This estimate compares favorably with SO_2 concentrations of 22.84 ± 2.3 and 57.1 ± 5.7 mg/m^3 measured near the rim of BN crater in 1978 and 1979, respectively (Jaeschke et al. 1982). Assuming a plume width of 1 km and a wind speed of 5 m/s, the

SO_2 concentrations derived from the TIMS data correspond to flux rates ranging between 5400 and 7600 tons/ day. These SO_2 flux rates are within the range of published flux rates from Mount Etna (cf. Haulet et al. 1977, Zettwoog and Haulet 1978, Malinconico 1979), but the TIMS-derived flux rates are higher than the average flux rates published in the literature.

The sensitivity of the estimation procedure to variations in the inputs to the LOWTRAN code was also evaluated. The estimation procedure was most sensitive to ground temperature; a 10 degree (Celsius) variation in ground temperature translated into a 50% change in the estimation of SO_2 concentration. Changes in the vertical distribution of SO_2 within the plume resulted in 20% changes in the estimates of concentration. Replacing the ground emissivity with a uniform value of 0.95 resulted in a 10% change in the estimates of concentration. The substitution of a climatological atmospheric profile (mid-latitude summer) for theTrapani radiosonde measurements resulted in a 20% change in the estimates of SO_2 concentration.

The TIMS data provided a near-instantaneous measurement of SO_2 concentration of the plume in the summit region of Mount Etna. Data such as these could aid in the study of temporal and spatial variations in the SO_2 content of the plume. It is recommended that future TIMS flights over venting volcanoes be accompanied by ground support crews. These personnel could collect ground temperature and emissivity measurements as well as launch radiosonde balloons. Despite the fact that the Mount Etna TIMS mission was not supported by a ground crew, the SO_2 concentrations derived from the TIMS data were in good agreement with published values. The availability of ancillary data can only improve the accuracy of the TIMS estimation procedure.

ACKNOWLEDGMENTS

The research described in this paper was conducted at the Jet Propulsion Laboratory, California Institute of Technology, under contract to the National Aeronautics and Space Administration.

REFERENCES CITED

Bianchi R, Casachia R, Coradioni A, Duncan AM, Guest JE, Kahle AB, Lanciano P, Pieri DC, Poscolieri M (1990) Remote Sensing of Italian Volcanoes. Trans Am Geophys Union 71: 1789-1791

Jaeschke W, Berresheim H, and Georgii H-W (1982) Sulfur emissions from Mt. Etna. J Geophys Res 87: 7253-7261

Haulet R, Zettwoog P, Sabroux JC (1977) Sulfur dioxide discharge from Mount Etna. Nature 268: 715-717

Malinconico LL (1979) Fluctuations in SO_2 emission during recent eruptions of Etna. Nature 278: 43-45

Realmuto VJ (1990) Separating the effects of temperature and emissivity: emissivity spectrum normalization. Proc Second TIMS Workshop, JPL Publ 90-55: 31-35

Smithsonian Institution (1986) Volcanic events: Etna. SEAN Bull (Sept 30) 11: 4-8

Warner TA, Levandowski DW (1990) Optimum band selections for estimating emittance using TIMS data. Proc Second TIMS Workshop, JPL Publ 90-55: 26-30

Zettwoog P, Haulet R (1978) Experimental results on the SO_2 transfer in the Mediterranean obtained with remote sensing devices. Atmos Environ 12: 795-796

Omit
Administrative

ATTIRE

(Analytical Tools For Thermal Infrared Engineering) - A thermal sensor simulation package

S. Jaggi

Lockheed Engineering & Sciences Company
Stennis Space Center, MS 39529

The Advanced Sensor Development Laboratory (ASDL) at the Stennis Space Center develops, maintains and calibrates remote sensing instruments for the National Aeronautics & Space Administration. To perform system design trade-offs, analysis, and establish system parameters, ASDL has developed a software package for analytical simulation of sensor systems. This package has been useful in modeling and analyzing the performance of various sensors such as the TIMS. This package called " Analytical Tools for Thermal InfraRed Engineering " - ATTIRE simulates the various components of a sensor system. The software allows each subsystem of the sensor to be analyzed independently for its performance. These performance parameters are then integrated to obtain system level information such as SNR, NER, NETD etc. This paper describes the uses of the package and the physics that were used to derive the performance parameters.

In addition, ATTIRE can be used as a tutorial for understanding the distribution of thermal flux or solar irradiance over selected bandwidths of the spectrum. This spectrally distributed incident flux can then be analyzed as it propagates through the subsystems that constitute the entire sensor. ATTIRE provides a variety of functions ranging from plotting black-body curves for varying bandwidths and computing the integral flux, to performing transfer function analysis of the sensor system.

The package runs from a menu-driven interface in a PC-DOS environment. Each sub-system of the sensor is represented by windows and icons. A user-friendly mouse-controlled point-and-click interface allows the user to simulate various aspects of a sensor.

The package can simulate a theoretical sensor system. Trade-off studies can be easily done by changing the appropriate parameters and monitoring the effect on the system performance. The package can provide plots of system performance versus any system parameter. A parameter (such as the entrance aperture of the optics) could be varied and its effect on another parameter (e.g., NETD) can be plotted. A third parameter (e.g., the obscuration) could be varied for each plot and several plots obtained on the same graph. The menu for such " Y vs X plots for different values of Z " currently contains various such options. The package also allows the user to create customized work-sheets of the simulated system and save the analysis for interface with or retrieval to other packages.

The emissivity, atmospheric transmission and the optical transmission default as constants over the specified spectral bandwidths. There is an option for making these parameters spectrally variable. If more than one of the above-mentioned three parameters are spectrally variable, then it is possible that the upper and lower wavelength values as well as the resolution of the wavelength array may not be the same for all three arrays. The package performs an interpolation of the data to smooth out the curves and then projects them onto a common wavelength array for all the parameters.

Overview

ATTIRE provides functions ranging from plotting blackbody curves and computing the integral flux, to performing radiation transfer function analysis and calculation of system performance parameters.

The package runs from a menu-driven interface in a PC-DOS environment. On executing the software, the user encounters a screen with a resizeable window and icons. The window contains the channels of the current multispectral sensor being analyzed. Each icon represents a sensor subsystem such as the optics, source flux, atmospherics etc. ATTIRE has a mouse-driven control for resizing or moving the windows within the screen. The mouse control also allows for the point-and-click feature making the package more user-friendly.

A horizontal menu within the window allows the user to change the parameters of the system. This menu contains items that allow the user to change the channel configuration, perform file I/O and do plotting operations. The number of channels is programmable through the horizontal menu item called CHAN. The bandwidths of each of these channels can also be varied from this menu-item. The entire sensor system can be saved as a worksheet in a file. This operation is done from the horizontal menu-item called FILE. The user can either retrieve an existing sensor system, save the current system or just browse through a system saved on disk before deciding to retrieve it.

The source emissivity, atmospheric transmission, and optical transmission are initially assumed constant over the specified spectral bandwidths. There is an option for making these parameters spectrally variable. If more than one of the above-mentioned three parameters are spectrally variable, then it is possible that the upper and lower wavelength values and the resolution of the wavelength array may not be the same for all three arrays. The software package performs an interpolation of the data to smooth out the curves and then projects them onto a common wavelength array.

The spectrally distributed incident flux can be analyzed as it propagates through the subsystems. Fig. 1 shows the signal flow and the various parameters that affect the performance of the system. Each of the icons on the main menu represent one of these sub-systems.

Summary

The design of a visible through thermal IR sensor system requires a detailed analysis of how the input signal propagates through the system. The major components in developing a model for the sensor system are the **source, atmosphere, optics, detector, spatial parameters,** and **preamplifier electronics.** The final goal of the analysis is to determine the NER for the various spectral channels of a sensor system.

In this paper, a simulation package "ATTIRE" for analyzing sensor systems was introduced. The package runs in a PC-DOS environment and consists of one executable program and several supporting files. The entire package fits on one high-density floppy disk.

ATTIRE is a useful tool for performing design tradeoffs as it interrelates several aspects of the sensor system to yield performance parameters. It is also useful as a tool for the understanding of the concepts of radiometry.

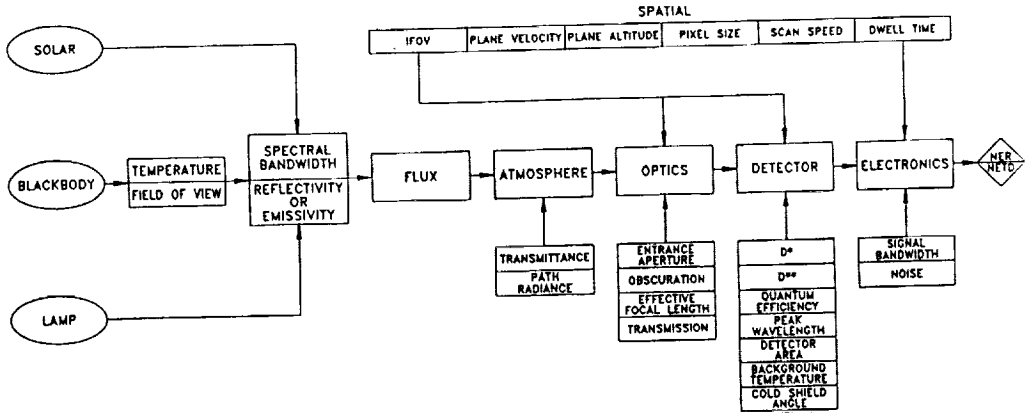

Fig. 1

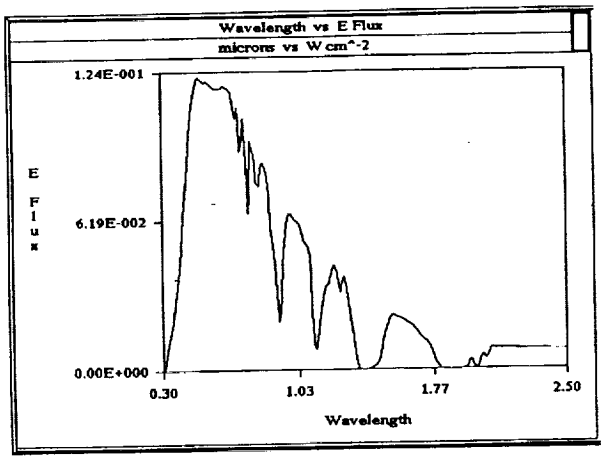

Fig. 2 Solar Curve used in ATTIRE

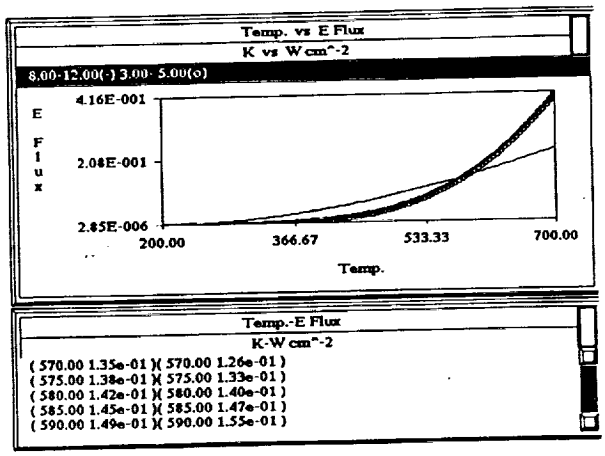

Fig. 3 Output from ATTIRE

omit
ADMINISTRATIVE

KILAUEA DATA SET COMPILED FOR DISTRIBUTION ON COMPACT DISC

Lori Glaze, George Karas, Sonia Chernobieff,
Elsa Abbott, and Earnie Paylor
Jet Propulsion Laboratory
California Institute of Technology
Pasadena, California

1. DATA COMPILATION

In the last several years, the NASA aircraft program has amassed a considerable set of remote sensing data. With the upcoming launch of the EOS instrument platform at the end of this decade, some type of mass data organization is necessary in order to efficiently archive both pre- and syn-EOS data. With this in mind, we have embarked on a series of Compact Disc volumes that will consist of data compilations for various areas. The first set in this series will be for Kilauea volcano on the island of Hawaii. Kilauea volcano makes up the southeast portion of the big island, and has been erupting along the east rift zone almost continuously since 1983.

Since 1985, the NASA C-130 aircraft has been deployed four times to the island of Hawaii. For each of these deployments, the complement of instruments included Zeiss metric cameras and the NS001 (Thematic Mapper Simulator) scanner, and all but the 1987 deployment also included the Thermal Infrared Multispectral Scanner (TIMS). Due to space restrictions, a single flight line of photographs for each area on Kilauea will be included on the disc, except in areas that underwent visible changes between deployments (i.e., the Pu'u O'o lava flow field). In addition to these C-130 data, the NASA DC 8 carrying the NASA/JPL Airborne multipolarization, multifrequency Synthetic Aperture Radar (AIRSAR) was deployed to Hawaii in 1990, mapping a large portion of Kilauea. The Compact Disc compilation will contain most of the useable data collected by these instruments over much of the volcano including multiple coverage of the active areas.

To aid in the use of the aircraft data, several other ancillary data types will also be included on the disc. These include a Digital Elevation Model (DEM) of Kilauea, and several maps showing the progression of lava flows over time provided courtesy of the U.S. Geological Survey/Hawaii Volcano Observatory. We will also include 'browse'

images of a Thematic Mapper scene and one or two NOAA AVHRR passes of the big island. Infrared laboratory spectra for many samples taken from various locations on Kilauea will also be included. The samples have been collected over several years during many different field campaigns.

2. DATA ORGANIZATION

The CDRom volume set will contain public domain image display software that is compatible with Sun Unix, PC and Macintosh operating systems. ReadMe files will be included for each data type explaining the data storage format as well as describing its possible uses. For some of the data types (i.e., TIMS), common data manipulation processes will be explained, and in a few cases, the algorithms will be provided.

The first disc in the set will contain examples of each of the data types. It will be designated as a sampler disc containing thoroughly processed versions of all data types covering two selected areas on the volcano. For these areas full color air photos and contrast enhanced NS001, decorrelation stretched TIMS, and fully processed SAR images will be provided for easy viewing.

The CDRom package is intended to provide a consolidated package of a sizable portion of the NASA aircraft acquired data for Kilauea volcano. The aircraft data, as well as the other types of ancillary data, will all be accessible in an easy to use format, in a single place. It is hoped that researchers from many disciplines working on Kilauea volcano will find this compilation useful.